Mössbauer Spectroscopy of Synthetic Olivine across the Mg-Fe Solid Solution

Elizabeth Christ Sklute
Mount Holyoke College

Advisor:
Professor M. Darby Dyar
Department of Astronomy, Mount Holyoke College

Acknowledgments

- My undying gratitude to Darby Dyar for her experience and support (emotional and financial) throughout this project. She introduced me to the fascinating world of Mössbauer spectroscopy and has taught me absolute necessity for unbiased scientific integrity. She is a true scientist and an amazing woman.
- Thank you to my family for supporting my scholastic whims.
- Thank you to Yarrow Rothstein, Claire Bendersky, Kylie Hanify, and Jerry Marchand for helping me change what seemed like an unending line of samples.
- I thank Catrina Hamilton-Drager and Mike Jercinovic for reviewing my thesis and hearing my defense.
- I am very grateful to Eddy De Grave, Toon Van Alboom, and David Agresti for their constant coaching on the underlying physics of this technique.
- And I am incredibly grateful to Donald Lindsley and Olwyn Menzies for the synthetic olivine samples that I was able to study.

Table of Contents

List of Tables and Figures

Abstract

Olivine is a major mineral component on terrestrial planetary surfaces and, therefore, it is important to understand its spectroscopic characteristics at all wavelengths. This study presents a detailed Mössbauer investigation of ten synthetic olivines in the fayalite-forsterite series (Fe_2SiO_4 – Mg_2SiO_4). Two distributions of Fe in olivine were consistently resolved. However, these doublets cannot be unambiguously assigned to Fe site occupancy in the M1 and M2 crystallographic sites in the olivine structure because their areas do not match known site occupancies. Moreover, these two doublets can be fit using two distinct models that yield different doublet area ratios yet are statistically indistinguishable in the spectra acquired at 13-293K. In all cases, isomer shift of the doublets is relatively constant across the entire solid solution, but quadrupole splitting correlates with composition (± 20% absolute) as QS = 0.000135x + 2.999 for a sample with composition Fo_x. The magnetic ordering temperature in olivine is also roughly linearly correlated with composition. Mössbauer spectra of olivine can appear very similar to those of some ferrous sulfates at low resolution and in mineral mixtures. Finally, recoil-free fraction values are not indicative of composition at a given temperature using our current method for their calculation.

Chapter 1

Introduction

The olivine mineral group includes the solid solution from fayalite (Fo_0: Fe_2SiO_4) to forsterite (Fo_{100}: Mg_2SiO_4) and is one of the most common rock-forming mineral groups on terrestrial planets. Occurring primarily in iron and magnesium rich igneous rocks, olivine is of particular significance in understanding planetary geology in differentiated bodies. Although extensive studies have been performed on olivine over a range of compositions (synthetic and natural), temperatures, and pressures, using a variety of methods (see Brown, 1980 for an excellent review), there is still a need for data on several aspects of olivine's nature and variation to create resolution over aspects therein. It has become even more imperative to understand olivine's structure and tendency since it was catalogued in abundance on the surface of Mars (Morris et al. 2004). In this study, we present a detailed Mössbauer spectroscopic analysis of ten synthetic olivines in the fayalite-forsterite series in the interest of answering several questions.

Perhaps the most pressing of these questions relates to the site preference of cations in the olivine structure. Olivine is a nesosilicate. In its structure, each oxygen ligand is bonded to only one silicon atom, creating discrete SiO_4

tetrahedra. These non-bridging oxygen atoms form two nonequivalent octahedrally coordinated sites in the olivine structure, designated M1 and M2 (M is for metal), into which divalent cations can fit (Figure 1.1). The M1 site is smaller than the M2 site by 0.03-0.05Å, and is the more distorted of the two sites (Lumpkin and Ribbe, 1983). The M1 site is roughly distorted into tetragonally elongated octahedron where the M2 site is approximately resembles a trigonally elongated octahedron (Burns, 1993).

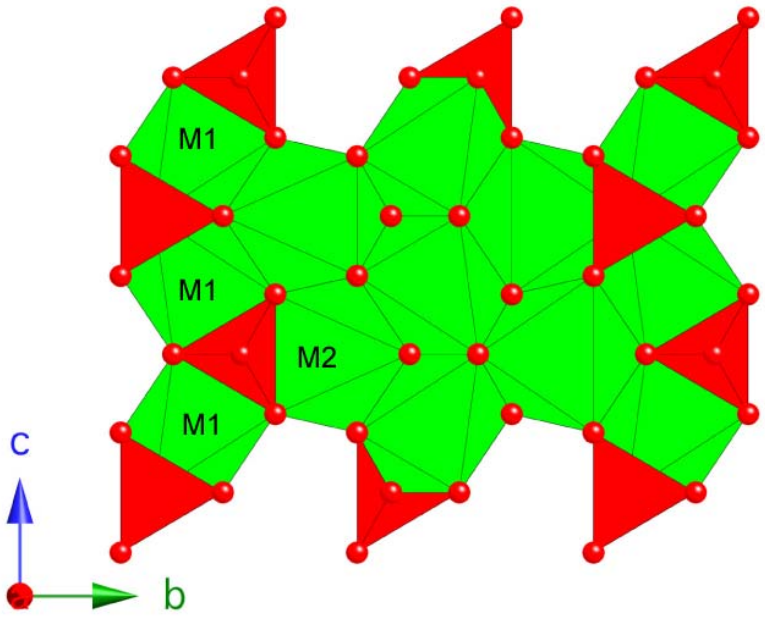

Figure 1.1; Olivine structure showing tetrahedra (red) and M1 and M2 octahedra. This figure was created by Mickey Gunter, to whom I am very grateful.

The difference in size and distortion of these two sites would seem to lead to a cationic site preference. To this date, there is evidence supporting both order and disorder, as well as data showing a preference for iron to be in both M1 and M2 (see Brown 1980 for a summary). The first major question in this study is,

therefore, what are the Mössbauer parameters corresponding to the M1 and M2 sites in olivine, and can those sites be consistently and systematically resolved? Cation distribution in olivine is dependent upon several competing factors.

- The cation with the larger ionic radius should prefer the larger octahedral site. In this case, the larger Fe^{2+} should prefer the larger M2 site.
- The two sites are not equally covalent in character; therefore, the cation with a greater electronegativity should go to the site that allows a greater degree of covalent bonding. This would create a preference for Fe^{2+} in the M1 site.
- Distortion of the M1 site leads to crystal-field stabilization energy (CFSE) which would have a greater stabilizing effect on the transition metal cation. This again predicts a preference for Fe^{2+} for the M1 site (Brown 1980).

In addition to these factors, cation distribution is sensitive to temperature, oxygen fugacity, composition, and pressure (Brown 1980). Throughout the literature, olivine studies show that while there is clear ordering in Mn-Fe^{2+} olivines (Annersten et al. 1984, Redfern et al. 1998), Ni-Mg olivines (Annersten et al. 1982, Ottonello et al. 1989), and Ni-Fe^{2+} olivines (Bish 1981, Rajamani et al. 1975), there are conflicting data as to if and how Mg and Fe^{2+} are ordered (Artioli et al. 1995, Brown & Prewitt 1973, Morozov et al. 2005, Nikitina 1982, Ottonello 1990, Princivalle 1990, Shinno et al. 1974,Virgo & Hafner 1972).

Although Mössbauer studies to determine cation partitioning in olivine have typically been limited to high temperatures up until this point, advances in Mössbauer spectrometers and fitting procedures may have made room temperature resolution of two distributions possible. In this study, the site assignment of the iron in olivine is investigated using a variety of fitting methods and over a range of temperatures.

The second major issue to be addressed here is the relationship between isomer shift, quadrupole splitting, and composition in the fayalite-forsterite series of olivine. It is not always possible to perform detailed compositional analyses of a sample (this is especially true for extraterrestrial samples analyzed *in situ*). Systematically linking the Mössbauer parameters of olivine with composition over a range of temperatures could provide a powerful diagnostic tool when temperature but not composition is known. The idea of linking quadrupole splitting to composition in olivine was first observed by Menzies and Bland in 2001. This aspect of the study stems from their work. It catalogues the changes of isomer shift and quadrupole splitting over the composition range from Fo_0 to $Fo_{89.5}$ to determine if there is such a systematic trend.

Third, how is the onset temperature of magnetic ordering related to olivine composition? The temperature at which a mineral's Mössbauer spectrum magnetically splits is a characteristic property of that mineral. Documenting the relationship between magnetic ordering temperature and composition in this solid-solution series would give greater insight into the way the olivine structure

changes with composition and temperature, as well as provide a useful diagnostic property if the relationship proves systematic. Here we investigate each of ten samples ranging from Fo_0 to $Fo_{89.5}$ from 13K to 293K to pinpoint the temperature at which each composition magnetically splits.

Fourth, how do the Mössbauer parameters for the M1 and M2 sites in olivine compare to the parameters for other ferromagnetic species? Characterization of Mössbauer spectroscopic parameters of olivine might allow olivine to be distinguished from other common minerals such as sulfates. This is important because the presence of different minerals can lead to very different conclusions about the origin and characterization of the host rock. Through a detailed documentation of olivine over multiple compositions and temperatures, this study provides a basis for comparison of olivine parameters with that of other ferromagnetic minerals.

Finally, what is the recoil-free fraction of olivine at varying temperatures and compositions? To compute the relative abundance of a mineral in a mixture such as a rock, it is necessary to know the recoil-free fraction for that mineral. Because minerals in nature usually coexist with other phases, recoil-free fraction values of rock-forming minerals are of great importance to Mössbauer spectroscopic studies of rocks, especially in situ. In this study, the recoil-free fraction values for olivine over a composition and temperature range are calculated.

The widespread occurrence and natural abundance of olivine mean that answering these questions will aid investigations in many fields. Olivine is a significant component in processes studied by petrologists, mineralogists, astronomers, and geochemists. A thorough investigation of olivine parameters over a range of compositions and temperatures will create a foothold from which other investigations can proceed and perhaps lead to other questions that will give us a fuller understanding of our terranean and subterranean world.

Chapter 2

Background

The goals of this chapter are to survey the theory and practice of Mössbauer spectroscopy as applied to the study of minerals, and to provide background on the olivine mineral group and previous studies of those species using Mössbauer spectroscopy. It includes a review of the scientific principles behind Mössbauer spectroscopy as well as a discussion of Mössbauer parameters and their implications for understanding mineral structures.

Mössbauer spectroscopy, or resonant gamma-ray emission/absorption spectroscopy, is the study of the interaction of electromagnetic radiation in the energy range from 10^4 to 10^5 eV (gamma radiation range) with atomic nuclei, specifically the fraction of recoilless resonant absorption and re-emission events in a solid, defined as the Mössbauer effect. The Mössbauer effect was discovered by Rudolf L. Mössbauer during his graduate studies in Heidelberg in 1957. The works of Frauenfelder (1962), who reviews early developments in Mössbauer spectroscopy, and Wegner (1965) who discusses its theoretical grounding, are useful for a fuller understanding of this subject. Greenwood and Gibb (1971) also provide an excellent review of the subject. It is the goal of this section to establish the necessary concepts required for interpreting the results of this study rather than to provide a report on the method itself.

Resonant Absorption

The processes of resonant absorption and emission of photons are familiar to many forms of spectroscopy. For example, when energy levels of 3*d* orbitals in transition metals split, photons of specific energies can excite an electron from one energy level to the other. When the atom returns to its ground state, it can emit a photon of the precise energy absorbed. The Mössbauer effect works directly from this principle with the exception that it deals with nuclear energy levels. To understand the analytical implications for Mössbauer spectroscopy, it is necessary to review some of the fundamentals of resonant absorption as they apply to the nucleus.

First, consider an isolated atom in a nuclear excited state with energy E_e (such as a radioactive isotope). The atom will decay and emit a gamma ray or transfer the energy in one of several competing processes that partition energy to an atomic electron (see Figure 2.3). If we assume that the emitted gamma photon takes away all of the excitation energy E_0, and encounters another, identical atom, it can be resonantly absorbed and then re-emitted.

Although it is customary to think of electronic energy levels as discrete, this precise quantization does not apply to nuclear energy levels because nuclear excitation has a finite lifetime Δt. The nuclear transition lifetime is therefore linked to nuclear transition energy by the Heisenberg uncertainty relation, such that

$$\Delta E \Delta t \geq \hbar \tag{2.1}$$

where ħ is Planck's constant divided by 2π. This relationship results in a finite distribution of energies for a nuclear transition that follows a Breit-Wigner, or Lorentzian distribution centered at E_0.

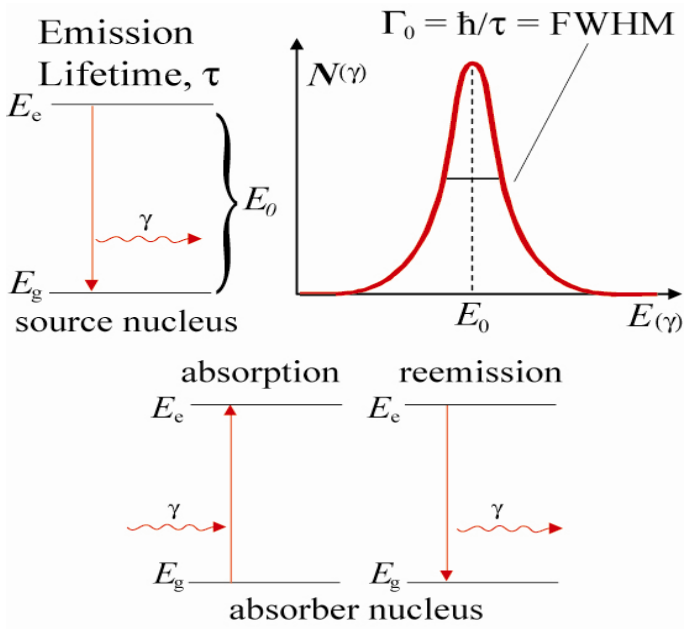

Figure 2.1; (Top) Idealized representation of nuclear resonance. The nuclear transition from the excited state E_e to the ground state E_g results in the emission of a gamma ray with an energy that obeys a Lorentzian distribution. (Bottom) A gamma ray incident on the absorber nucleus causes a transition from the nuclear ground state to the excited state. The absorber nucleus returns to its ground state by re-emitting an identical gamma ray.

If it is assumed that $\Delta t = \tau$, the energy of the distribution can be related to its full width at half maximum Γ_0 (Figure 2.1) by

$$E_0 = \Gamma_0 = \hbar/\tau \ . \tag{2.2}$$

The model thus far has assumed that the entire energy of the nuclear transition is carried away by the gamma photon, i.e., $E_\gamma = E_0$. However, the gamma photon has momentum

$$p_\gamma = \frac{E_\gamma}{c}, \tag{2.3}$$

where c is the speed of light in a vacuum. If the emitting atom is initially at rest, then by conservation of momentum, the nucleus must recoil with equal and opposite momentum to the gamma photon: $p_{\text{nucleus}} = -p_\gamma$. The emitting nucleus thus gains recoil energy

$$E_R = \frac{(p_{\text{nucleus}})^2}{2M} = \frac{(-p_\gamma)^2}{2M} = \frac{E_\gamma^2}{2Mc^2}, \tag{2.4}$$

where M is the mass of the emitting nucleus. By conservation of energy ($E_{\text{initial}} = E_{\text{final}}$), the nuclear excitation energy must be shared between the nuclear recoil and the emitted photon, such that

$$E_0 = E_\gamma + E_R \Leftrightarrow E_\gamma = E_0 - E_R. \tag{2.5}$$

So for the case of the emitting atom, the energy of the gamma photon is decreased by the recoil energy of the emitting nucleus.

Now consider the absorber. If again it is assumed that the atom is initially isolated and at rest, then by a similar argument to that for the source nucleus, the absorber will experience recoil E_R such that,

$$E_\gamma = E_0 + E_R. \tag{2.6}$$

In other words, the incident gamma photon must be of sufficient energy to both excite the nuclear transition and to allow for nuclear recoil.

Recoil energy is typically on the order of 10^{-4}–10^{-1}eV (Greenwood & Gibb 1971), which seems insignificant when compared to the energy of a gamma

photon (10^4-10^5eV). However, the Heisenberg natural linewidth (FWHM, Figure 2.1) is considerably smaller (10^{-9}-10^{-6}eV) than the recoil energy. Therefore, resonant gamma emission and absorption cannot happen between two isolated atoms at rest. Figure 2.2 shows the Lorentzian distributions for the emitting and absorbing atoms. These energy distributions must overlap in order for resonant absorption to occur. Note that the overlap (which is greatly exaggerated in this figure) is only slight between the two distributions.

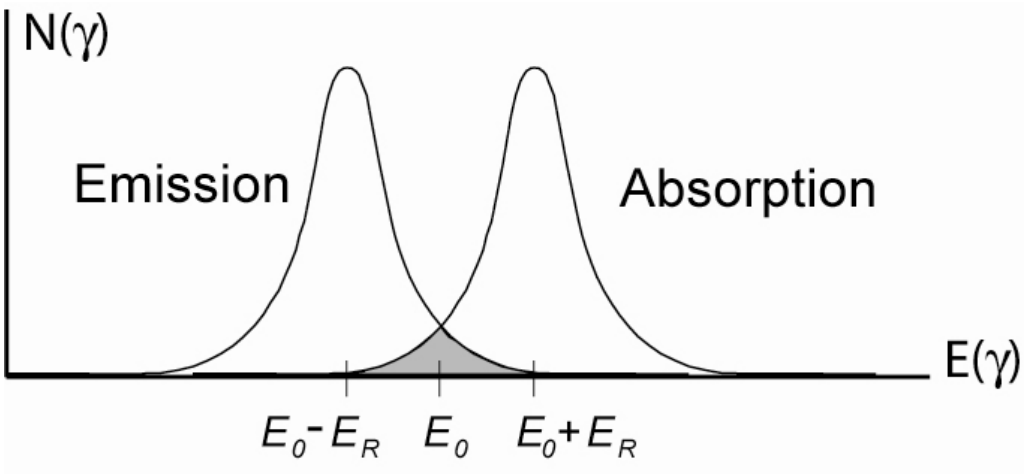

Figure 2.2; Lorentzian distributions of emitting and absorbing nucleus. The degree of overlap reflects the percentage of resonant gamma emission and re-absorption events. Note that the degree of overlap is greatly exaggerated.

The theoretical discussion up to this point has assumed that the atoms were initially at rest. This is not the case in nature. Whether in solid, liquid, or gas, atoms experience a degree of thermal vibration on the order of k_BT, where k_B is Boltzmann's constant and T is the temperature in Kelvin. This thermal vibration at room temperature (300K) is approximately 0.025 eV (Dyar et al. 2006), which is on the same order of magnitude as E_R. Depending on the

direction of motion of the atom, the atomic vibration can add or subtract a Doppler energy to the atom. This added energy broadens the Lorentzian distribution for both the emitting and absorbing atoms, making resonant emission and absorption of gamma rays theoretically possible for two isolated atoms possessing thermal vibrational energy. However, due to the dependence of vibrational energy on temperature, absorption should decrease with decreasing temperature. This is in fact what Mössbauer himself observed. He found, though, that when temperature dropped to that of liquid nitrogen (~63-77K), absorption increased significantly (Mössbauer 1958).

This increase in absorption is based on complicated processes that are not relevant to this discussion because it turns out that Doppler broadening was not the key to the Mössbauer Effect. It can, however, play a part in errors associated with Mössbauer spectra. In fact, the Mössbauer effect originates from the special properties of atoms in a solid and the ways in which energy can be transferred to and within that solid. A simplified version of the reasoning is presented here; for a full theoretical treatment of the subject, refer to Mössbauer (1958) and Visscher (1960).

In a liquid or a gas, atoms can vibrate completely independently of one another, and they can also possess independent kinetic motion. In a solid, however, atoms are bound, decreasing the amount of independent vibration but creating group vibrational modes that can be treated through quantum mechanics as harmonic oscillations. Using a simple Einstein model for quantization, a single

vibrational frequency, ω, is characteristic of each vibrational mode. We can thus quantify the energy associated with each harmonic mode by

$$E_{SHM} = (n + ½)\hbar\omega. \quad (2.7)$$

Here $n = 1, 2, \ldots$ is the vibrational quantum number. It is clear from the expression that the energy of the solid is quantized. The discrete energy units that can be accepted to excite a solid have been labeled phonons, and the phonon mode is equal to the vibrational quantum number n.

A further simplification can be applied to the Einstein model so that only one frequency, ω, is considered. If it is assumed that $E_R < \hbar\omega$, and that when a gamma photon is emitted either n stays constant (a zero-phonon event), or n increases by 1 (a one-phonon event), then f can be defined as the fraction of zero-phonon events relative to one-phonon events. The average energy received by the crystal can thus be written as

$$E_{average} = (1 - f)\,\hbar\omega. \quad (2.8)$$

In the case of zero-phonon transitions, the recoil momentum is distributed across the entire solid. The large mass of the solid is then plugged into the equation for recoil energy (Equation 2.4). Because the recoil energy and mass are inversely proportional, the recoil energy in the zero-phonon case can be considered negligible.

Lipkin (1960) showed through a theoretical consideration of gamma-ray emitting crystal lattice structures that $E_{average} = E_R$ when a large numbers of

gamma-ray emission events are considered. Therefore, the equation above becomes

$$E_R = (1 - f)\,\hbar\omega \Leftrightarrow \tag{2.9}$$

$$f = 1 - E_R/\hbar\omega. \tag{2.10}$$

We can see from equations (2.10) and (2.4) that in order to maximize the recoil-free fraction (and make the Mössbauer Effect as big as possible), ħω must be maximized and/or E_R must be minimized (E_γ is minimized). To see the correlations for the solid that come from maximizing *f* more clearly, the equation to calculate *f* can be analyzed. However, in getting to Equation 2.10, many assumptions have already been made to make the crystal structure more mathematically simple to model. It may be prudent, therefore, to consider a general formula that is independent of the vibrational model for the solid. Equation (2.11) relates the recoil-free fraction to the vibrational properties of the solid lattice by

$$f = \exp\left[-\langle x^2\rangle E_\gamma^2 / (\hbar c)^2\right], \tag{2.11}$$

where *x* is the displacement of the nucleus from its equilibrium position in the direction of the emitted or absorbed gamma photon and $\langle x^2\rangle$ is the mean-squared displacement or the mean-squared vibrational amplitude (Dyar 2006). It is evident from Equation 2.11 that *f* is dependent upon the rigidity of the atoms in a lattice, which leads to two conclusions: *f* will be larger for more tightly bound atoms and *f* will decrease with increasing temperatures. It is, however, impractical to evaluate *f* using equation (2.11) because the $\langle x^2\rangle$ term is dependent

upon vibrational properties of the lattice that are complex to ascertain and calculate. The most common approximation for this calculation is the Debye model, which assumes a continuum of vibrational frequencies. In this model, the recoil-free fraction is calculated by

$$f = \exp\left\{-\frac{6E_R}{k\theta_D}\left[\frac{1}{4}+\left(\frac{T}{\theta_D}\right)^2\int_0^{\theta_D/T}\frac{x\,dx}{e^x-1}\right]\right\}. \qquad (2.12)$$

Here, θ_D is the Debye temperature, a characteristic of the rigidity of the lattice, and θ_D will be proportional to the maximum vibrational frequency of that lattice.

Even though the best theoretical model was chosen, this method is based upon assumptions. Real atomic and molecular systems are so complex that assumptions must be made in order to theoretically evaluate them. Each approximation falls short in its own way. It has been noted that the Debye model is inadequate even in dealing with simple real systems (Leibfried and Brenig 1953). This is, however, an accepted method used for such calculations and has been used by many others (e.g., Amthauer et al. 1976, Rancourt 1989, De Grave et al. 1985, De Grave and van Alboom 1991), thereby making the recoil-free fractions and Debye temperatures presented in this thesis of value at least by comparison to those of previous workers.

Mössbauer Spectroscopy using ^{57}Fe

Mössbauer spectroscopy can be performed using any nuclide. However, the discussion above showed that for the best results (largest recoil-free fraction value), several considerations must be made in choosing a source nuclide. First, E_γ, which is the energy of the nuclear transition, should be as small as possible to minimize E_R and maximize f. Second, the transition lifetime, τ, which determines the width of the energy distribution, should be small enough (the distribution wide enough) that there is no undue vibrational sensitivity, yet large enough (distribution narrow enough) that resolution is not compromised. Third, since the source nuclide determines the element that is observed (they must be the same in order for resonant absorption to occur), it must be an element that is common and abundant enough that investigations have scientific relevancy and interest.

Iron is particularly well suited to this task. It is not only the most commonly occurring multivalent element on earth (and other terrestrial planets); it also meets the other criteria readily. In fact, the majority of Mössbauer spectroscopy is done using ^{57}Fe as a source. Iron makes up approximately 5% of the Earth's crust. Of that, 2.2% is the ^{57}Fe isotope but its transition lifetime and recoil-free fraction value make up for this small percentage to yield high quality Mössbauer measurements. The f value for ^{57}Fe is quite large at ~0.65-1 and the transition lifetime for the relevant 14.4-keV excited state is 141 ns.

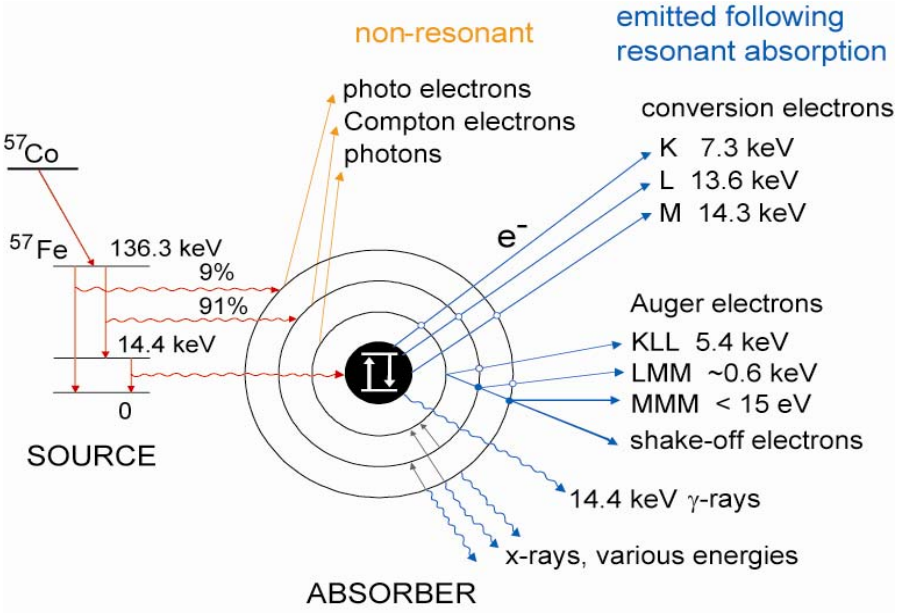

Figure 2.3; Schematic of nuclear decay from ^{57}Co to ^{57}Fe and various emission processes for ^{57}Fe that follow resonant absorption.

Figure 2.3 shows a schematic for the energetic processes of ^{57}Fe that are relevant in the investigation of minerals. The parent isotope ^{57}Co has a half-life of 270 days. It decays primarily to the 136.3-keV level of ^{57}Fe. This is an excited state for ^{57}Fe and it can return to its ground state through two processes. About 9% of the time, it returns directly to ground emitting a 136.3-keV gamma photon. The rest of the time, it drops first to the 14.4-keV excited state and then to the ground state, emitting a gamma photon of 14.4-keV ~11% of the time. The other 89% of de-excitation events through this intermediate excited state are documented in Figure 2.3. Although the other events should be noted as important for other forms of spectroscopy, they will not be discussed here because they are not relevant to this particular study.

The Mössbauer Spectrometer

The most common experimental geometry for measurement of the Mössbauer effect, as used in this study, is transmission spectroscopy. Figure 2.4 shows a typical configuration for a Mössbauer transmission experiment. For an in-depth explanation of the instrumentation, see Bancroft (1973) and Murad and Cashion (2004).

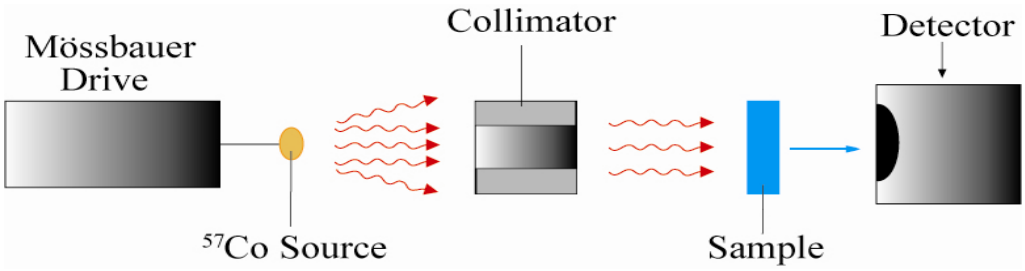

Figure 2.4; Diagram of transmission Mössbauer spectrometer. Gamma rays from the source are collimated and then passed through the sample. The detector records the number of gamma photons that are transmitted through the sample (are not absorbed).

In Mössbauer transmission spectroscopy, gamma rays from a radioactive source are collimated and then passed through a sample. The attenuation of the beam of gamma rays (the decrease in its intensity) is measured. The degree of attenuation is representative of the amount of overlap between the Lorentzian distributions for the source and the absorber. A large degree of overlap implies that the energy of the emitted gamma photon is the same as the energy required for that photon to be absorbed a large percentage of the time. The result is that a significant percentage of the gamma photons is absorbed and the percent transmitted to the detector is quite small. It should be noted here that although it

is possible for the detector to register gamma photons that have been absorbed and re-emitted, these gamma photons would be re-emitted isotropically. So, the number of such events that reach the detector is insignificant compared to the amount of collimated gamma photons that pass through the sample.

The experiment that has been described only produces one value - the percent transmission after the gamma ray beam passes through the sample. This value is not of particular scientific interest. It also does not allow for significant energetic differences between the source and absorber. If, however, it was possible to look at a range of transmission values, then data that are more meaningful could be acquired and these possible energetic differences could be explored. To examine a range of values, all that is needed is to add a slight Doppler velocity to the source by oscillating the Mössbauer drive. This oscillation modifies the gamma emission energy such that the transmission values for $E_0 - \delta E_0$ to $E_0 + \delta E_0$ can be observed. The resultant spectrum is a graph of transmission versus Doppler velocity. Figure 2.5 is a schematic of how a Mössbauer spectrum is acquired from this added Doppler shift. The absorber observes gamma photons with energies that vary in proportion to the degree of Doppler shift. Therefore, the amount of overlap between the source and the absorber changes with the same proportionality, finally producing the curve seen at the bottom right of the figure.

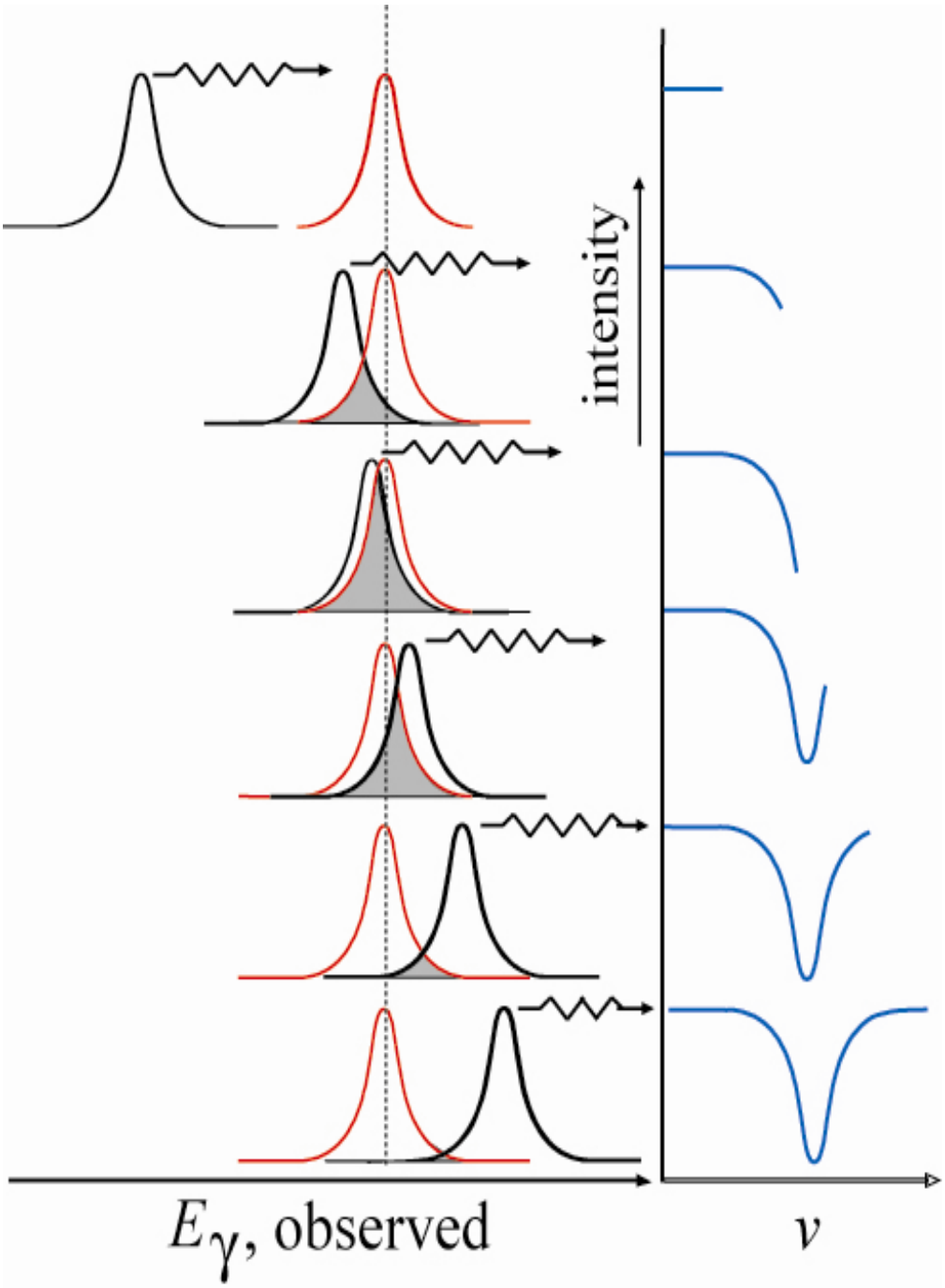

Figure 2.5; Schematic of acquisition of Mössbauer spectrum. The source is moved by a Doppler velocity, creating an overlap of the source and absorber energy distributions. When there is no overlap, the Mössbauer spectrum shows 100% transmission (0% absorption). As more overlap is created by the Doppler velocity, fewer gamma rays get through to the detector, creating a drop in absorption that forms the peak in the spectrum.

Mössbauer Spectra and Parameters

Throughout the discussion thus far, we have assumed that the atoms in question were identical. This is not true and would prove uninteresting for study, because the absorption and emission energies would be similar and predictable through theoretical means. In nature, the electronic state of the atom and the environment of the atom both affect the energy of the nuclear transition. It is these differences that the Mössbauer parameters describe.

Isomer Shift

If the local environments of the source and absorber are identical, then the energy required to excite the transition in the absorber is the same as that emitted from the source. The result is a minimum transmission (or maximum absorption) when no Doppler velocity is added to the source. This point is marked as zero velocity on the spectrum. If, however, as is true in most investigations, the local environment of the absorber is different from that of the source, then the maximum absorption point is shifted from this zero position by an amount that is characteristic of the environment of the iron in the absorber. This shift is known as isomer shift or center shift. It is recorded in mm/s, and is denoted by IS, CS, or δ (Figure 2.6 blue).

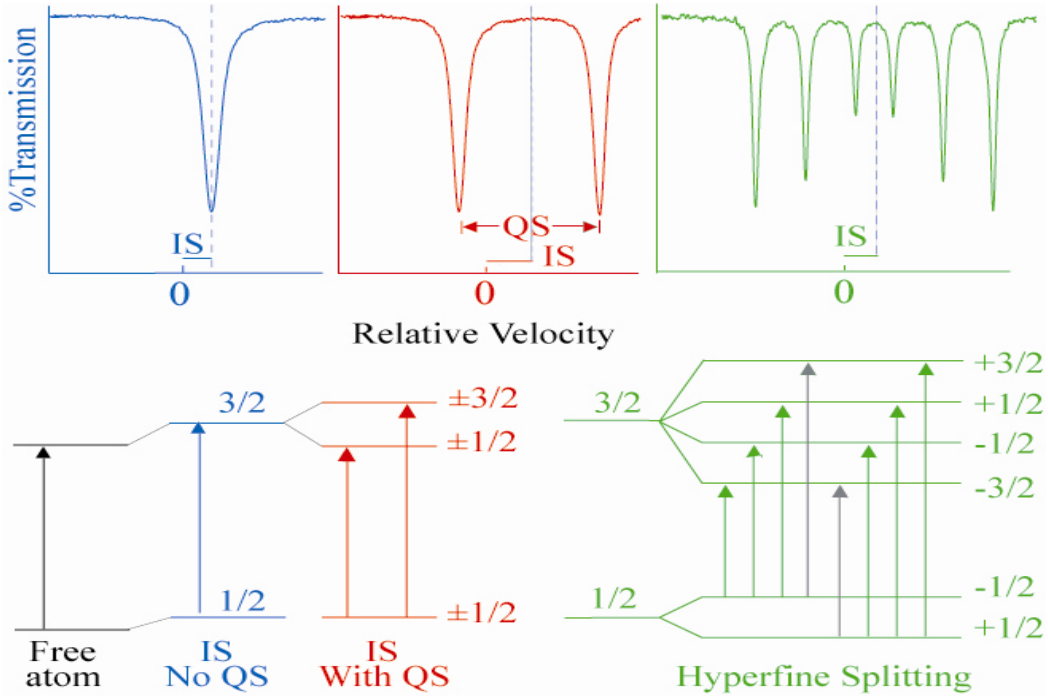

Figure 2.6; Different local environments around atomic nuclei result in energy differences. The simplest case produces a velocity shift of the peak in the transmission spectrum (blue), called an isomer shift and denoted by IS. The notations 1/2 and 3/2 refer to the nuclear spin, or angular momentum quantum numbers I. When the quadrupole moment at the nucleus interacts with the electric field gradient at the nucleus, it causes the ^{57}Fe Mössbauer spectrum to show a doublet. The phenomenon is called quadrupole splitting and is denoted by QS (red). If there is a magnetic field present at the nucleus, then hyperfine or Zeeman splitting takes place in the nuclear energy levels, producing a sextet in the Mössbauer spectrum (green). The arrows in gray represent transitions that are disallowed by the selection rule $|\Delta m_I| \leq 1$. In most simple cases, the area ratios of the remaining peaks are 3:2:1:1:2:3. Note that the arrow lengths indicating the transitions are shortened so that the splitting can be seen clearly.

Isomer shift arises because the nucleus, which in theory possesses fixed energy levels, is capable of interacting electrostatically with the surrounding charge density. For the case in which the nucleus can be treated as perfectly spherical, and the surrounding charge density is uniform, Coulombic interaction between the nucleus and the surrounding charge density changes the nuclear radii of the ground and excited (isomeric) states. These differences in nuclear radii

change the energy of the ground to excited state transition. The result is an isomer shift relative to some standard (usually α-Fe, although sodium nitroprusside is sometimes used). In a Mössbauer spectrum, isomer shift is observed where the Doppler velocity applied to the source correctly modifies the source's gamma rays energy to account for the difference between the source and the absorber.

The *s* electron charge density affects the nucleus most prominently, but shielding effects from the *p*, *d*, and *f* orbitals, as well as binding interactions of these orbitals, also contribute to the electronic environment. As a result, isomer shift is sensitive to differences in oxidation state, spin state, covalency, and coordination environment (number and type of bonded ligands).

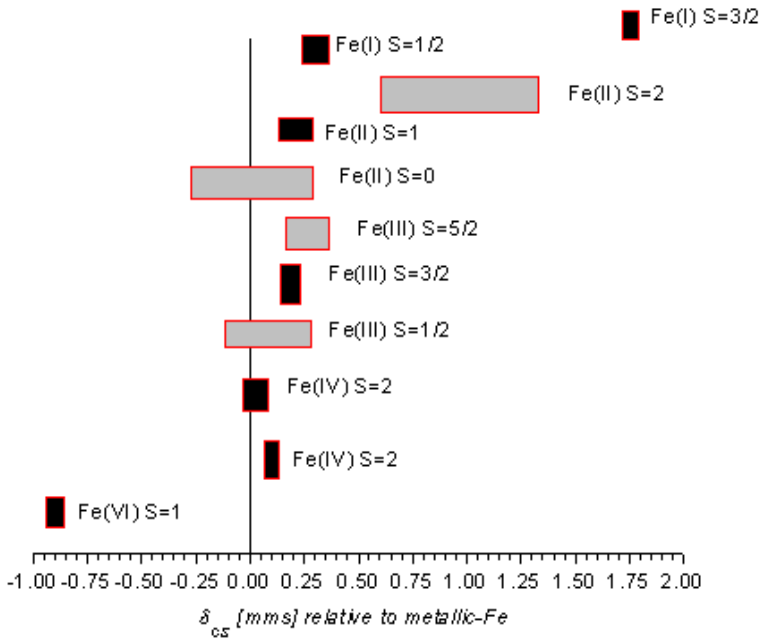

Figure 2.7; Distribution of isomer shift ranges with respect to spin and oxidation state. Figure taken from Greenwood (1971).

Figure 2.7 shows the variation of isomer shift with respect to oxidation and spin state. In general, Fe^{3+} has a lower isomer shift than Fe^{2+}.

Although isomer shift itself is not temperature dependent, the non-zero mean squared velocity of the nuclei results in a change of isomer shift with temperature. This phenomenon is known as a second order Doppler shift, and is typically denoted by δ_{SOD}. Isomer shift then becomes

$$\delta(T) = \delta_1 + \delta_{SOD}(T) \tag{2.13}$$

or

$$\delta(T) = \delta_1 - \frac{9}{2}\frac{k_B T}{Mc}\left(\frac{T}{\Theta_M}\right)^3 \int_0^{\Theta_M/T} \frac{x^3 dx}{e^x - 1}, \tag{2.14}$$

where δ_1 is the intrinsic isomer shift (a constant) and Θ_M is the characteristic Mössbauer temperature. Looking back to equation 2.12, it is clear that once Θ_D (labeled Θ_M for Mössbauer) is known, the recoil-free fraction, *f*, can be calculated for any temperature. Thus, Mössbauer studies of a sample over a range of temperatures provide a means of calculating recoil-free fractions.

Quadrupole Splitting

When the quantum spin number, *I*, is greater than 1 in the nucleus (Figure 2.6 red), there is no longer nuclear spherical symmetry. This asymmetry creates a quadrupole moment in the nucleus that is capable of interacting with the electric field gradient (EFG) created by other charges in the crystal. This interaction

partially removes the $(2I + 1)$-fold degeneracy of the nuclear energy states, causing the $I = 3/2$ nuclear energy level to split. The phenomenon is called quadrupole splitting and is denoted by QS, Δ, or ΔE_Q. The result is two peaks (a doublet) instead of one in the Mössbauer spectrum. Quadrupole splitting is the distance between the two peaks, which corresponds to the energy difference between the split states. By comparison, isomer shift for a doublet is the shift from zero mm/s of the center point between the two peaks. Together, these two parameters define the peak locations in a doublet in a superparamagnetic solid.

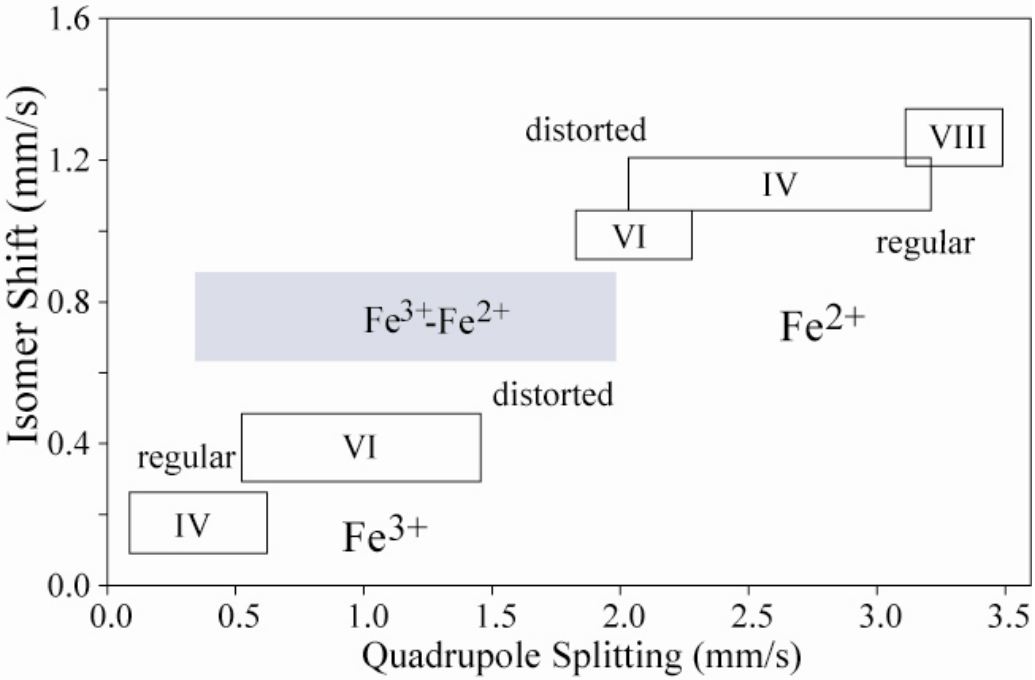

Figure 2.8; Isomer shift and quadrupole splitting ranges for various coordination environments and oxidation states. The ranges are fairly distinctive for different valence and oxidation states of iron. The blue box at the center of the graph with 0.5<IS<0.9 represents a range usually attributed to delocalized electrons between adjacent Fe^{2+} and Fe^{3+} atoms, resulting in averaged isomer shift and quadrupole splitting values.

Quadrupole splitting, like isomer shift, is sensitive to the coordination number and oxidation state of the atom because it, too, results from changes in the local electronic environment. Figure 2.8 shows the variation of quadrupole splitting and isomer shift with coordination number and oxidation state.

Magnetic Hyperfine Field Interactions

There is a magnetic moment associated with the ^{57}Fe nucleus that is caused by an interaction between the nucleus and its electrons. This magnetic moment can interact with external magnetic fields that originate from the structure of the iron-bearing mineral or those applied. The result is a complete loss of degeneracy in the energy levels of the ^{57}Fe nucleus, causing 6-8 peaks to appear in the spectrum instead of one or two (Figure 2.6 green). This is called magnetic hyperfine interaction or Zeeman interaction. In most cases, selection rules for nuclear energy level transitions exist ($|\Delta m_I| \leq 1$), forbidding the transitions from I=1/2 to I=-3/2 and I=-1/2 to I=3/2, such as in Fe foil. In some cases, however, these transitions are actually observed, creating eight peaks instead of six. This is the case with low temperature rozenite spectra, for instance.

The isomer shift value for a magnetically split spectrum is the shift from zero of the center of the inner most peaks of the sextet/octet. The QS value for such a spectrum is no longer the quadrupole splitting (even thought the symbols

are the same), but instead is termed the quadrupole shift. In the simplest case, this value can be calculated as $QS = (l_6-l_5)-(l_2-l_1)$, where l_i is the line position of a single peak. Complications arise because there is no closed form expression that calculates both magnetic field interactions and quadrupole splitting interactions. The two parameters are related, however, through the relative geometries of the EFG, effective magnetic field (H_{eff}), and the crystal symmetry (Figure 2.9).

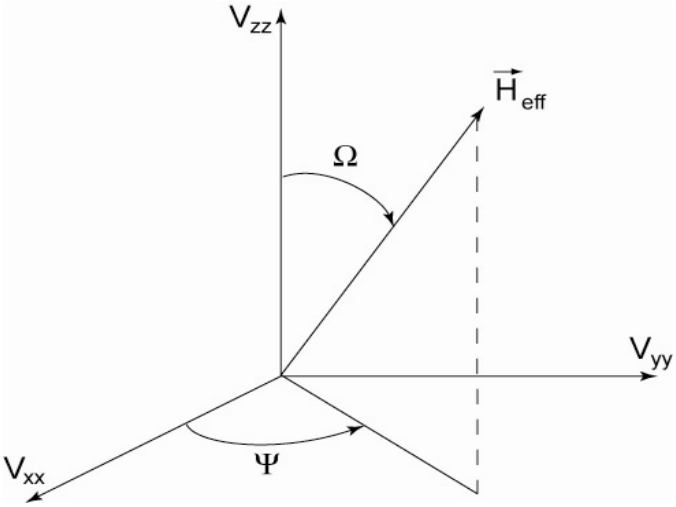

Figure 2.9; Schematic of EFG axes and their geometric relationship to the effective magnetic field at the nucleus of the absorber.

The parameters that describe a magnetically split spectrum are, therefore, more complex. B_{Hf} is the magnitude of the effective magnetic field (reported in Tesla or kOe, which differ only by a factor of 10). The angle between the V_{zz} axis of the EFG and H_{eff} is defined by Ω, and the angle between the V_{xx} axis of the EFG and the projection of H_{eff} onto the V_{xx}-V_{yy} plane is given by ψ. The asymmetry parameter eta, η, given by

$$\eta = (V_{xx} - V_{yy})/V_{zz}, \tag{2.15}$$

is one of the two parameters needed to define the EFG. The other is either V_{zz}, V_{xx}, or V_{yy}. The EFG axes are typically chosen so that $|V_{zz}| > |V_{xx}| \geq |V_{yy}|$, making $0 \leq \eta \leq 1$. For a doublet, η is usually zero, so this parameter is not used in those cases. In an ideal thin absorber (one in which there are negligible thickness effects), the ratio of the sextet peaks is 3:2:1:1:2:3 and the widths of all peaks are assumed to be the same.

Not all fitting programs calculate all of these parameters. Many only calculate B_{HF}, QS, IS and Γ. Some allow area ratios to vary and some provide even more fitting variables. The variables discussed here are those determined by fitting programs Mexfieldd and Mexdisdd, used in this study for magnetically split spectra. For a comprehensive mathematical review of Mössbauer parameters, refer to Wertheim (1968).

Width

The width of a spectral peak is unavoidably connected to the way in which energy passes through the sample; specifically, the way in which gamma radiation attenuates as it encounters successive Fe atoms. In the general case, this saturation effect arises from the fact that once light has encountered its first atom, and specific wavelengths are absorbed, the light is no longer “white” or representative of the full electromagnetic spectrum. The result is that there is not a direct proportionality between the decrease in intensity of light transmitted

through the entire sample and the increase in the thickness of that sample. For Mössbauer spectroscopy (remember that there is also an energetic distribution of the gamma rays coming from the source because of the Heisenberg uncertainty relation and the added Doppler velocity) this lack of proportionality is called the thickness effect and results in a change in lineshape, which translates to a change in width values. Because width values are directly linked to relative areas of spectral components, erroneous area ratios result from failing to correct for these thickness effects.

The FWHM calculation in equation 2.2 relies upon the assumption that the lineshape in the Mössbauer spectrum is perfectly Lorentzian. That Lorentzian lineshape comes from a mathematical simplification called the thin absorber approximation, which states that

$$fna\sigma_0 t >> 1 \qquad (2.16)$$

for both the source and the absorber. Here f is the recoil-free fraction, n is the number of atoms per volume element, a is the fractional abundance of the Mössbauer nuclide, and t is the physical thickness of the source or absorber (See Grant, 1995 for a more in-depth mathematical review of this assumption). Unfortunately, this thin absorber assumption rarely holds in real samples. There is a trade-off between using a small enough sample to ensure that the thin absorber approximation holds and using sufficient sample for reasonably short run times.

Mössbauer Parameters and Mineral/Site Identification

As shown above in Figures 2.7 and 2.8, Mössbauer parameters of Fe^{2+} and Fe^{3+} iron are quite distinctive. This characteristic, when combined with the low sample weight requirement (typically 10-40 mg, but samples have been successfully run with as little as 1 mg), makes Mössbauer spectroscopy the leading method for determining Fe^{3+}/Fe^{2+} ratios in minerals. The coordination number of iron in minerals is also fairly easy to determine in high count rate spectra. The challenges in using Mössbauer parameters for mineral and iron site identification are two-fold. First, in spectra with multiple doublets, or mixtures of doublets and sextets, overlap between peaks can cause significant error bars and non-uniqueness in the parameters. In other words, there is more than one possible best fit for most spectra. Second, the range of Fe^{2+} and Fe^{3+} isomer shifts and quadrupole splitting values is not that large (especially for Fe^{2+} isomer shifts), meaning that many samples containing Fe^{2+} iron have very similar isomer shift and quadrupole splitting values. These two factors limit the use of Mössbauer spectroscopy as an independent tool for mineral and site identification. Mössbauer spectroscopy, when used with other forms of spectroscopy, is a powerful constraint on mineral identification but use of Mössbauer alone to make identifications is impractical. Mineralogists and geologists typically use x-ray diffraction, which is far less subject to interpretation, for unequivocal mineral identification.

Mössbauer Parameters for Olivine

The crystal chemistry of olivine has been of interest for eighty years. The first structural work was performed by Bragg and Brown (1926) on a natural $Fo_{90}Fa_{10}$ crystal. Ghose (1962) made the first predictions describing the distribution of Fe and Mg between the two octahedral sites (M1 and M2) in the olivine structure. Since then, numerous experiments have been performed on synthetic and natural olivine samples, using a variety of techniques, and over a range of temperatures, pressures, and compositions. Below is a table summarizing the olivine Mössbauer parameters from many of these studies.

Table2.1; Mössbauer parameters for olivine from previous works. Here δ is isomer shift, Δ is quadrupole splitting, and Γ is peak width or FWHM of the fitted distribution.

Bush, Hafner, and Virgo (1970)								
Sample	Chemical Comp.	Temp (K)	δ (mm/s)		Δ (mm/s)		Γ (mm/s)	
			1	2	1	2	1	2
Ho-A	$Fo_{26}Fa_{74}$	588	1.03	0.89	2.41	2.14	0.297	0.286
Ho-A	$Fo_{26}Fa_{74}$	843	0.86	0.72	1.95	1.67	0.291	0.302
B1	$Fo_{82}Fa_{18}$	588	1.01	0.90	2.47	2.25	0.313	0.276
B1	$Fo_{82}Fa_{18}$	828	0.85	0.73	2.01	1.77	0.321	0.288
B1	$Fo_{82}Fa_{18}$	923	0.78	0.67	1.85	1.62	0.325	0.301

Malysheva, Kurash, and Yermakov (1969)							
mol % FeO	Temp (K)	δ (mm/s)		Δ (mm/s)		Γ (mm/s) L-R	Dist. I/II
7	300	1.28±0.02		3.02±0.02		0.58-0.65	
		I	II	I	II		
	550	1.04±0.03	1.24±0.03	2.26±0.03	2.66±0.03	0.60-0.75	0.53/0.47
50	300	1.28±0.02		2.94±0.02		0.57-0.57	
	450	1.16±0.03		2.60±0.03		0.62-0.63	
		I	II	I	II		
	550	1.02±0.03	1.16±0.03	2.32±0.03	2.60±0.03	0.60-0.68	0.50/0.50

Shinno (1974)							
Sample no.	Temp (K)	δ (mm/s)		Δ (mm/s)		Γ (mm/s)	
		M1	M2	M1	M2	M1	M2
Fa-1-A	RT	1.40	1.43	2.83	3.16	0.44	0.37
Fa-1-B	373	1.25	1.31	2.57	2.91	0.27	0.27
Fa-1-C	443	1.26	1.32	2.25	2.65	0.25	0.26
Fa-1-D	473	1.28	1.33	2.22	2.65	0.16	0.25
Fa-1-E	523	1.24	1.29	2.15	2.60	0.26	0.25
Fa-1-F	573	1.18	1.24	1.99	2.46	0.26	0.26
Fa-1-G	623	1.12	1.18	1.82	2.32	0.23	0.26
Fa-1-H	583	1.07	1.09	1.88	2.33	0.46	0.38
Fa-1-I	688	1.20	1.26	1.82	2.30	0.31	0.35
Fa-1-J	663	1.17	1.22	1.77	2.23	0.25	0.25
Fo507-A	RT	1.44	1.47	2.88	3.08	0.31	0.17
Fo507-B	373	1.34	1.40	2.66	2.90	0.35	0.20
Fo507-C	454	1.26	1.32	2.34	2.71	0.34	0.26
Fo507-D	488	1.24	1.31	2.26	2.64	0.34	0.23
Fo507-E	523	1.25	1.31	2.27	2.69	0.37	0.33
Fo507-F	653	1.17	1.24	2.00	2.40	0.27	0.26
Fo507-G	663	1.15	1.20	2.02	2.44	0.27	0.26
Fo507-H	703	1.10	1.17	1.87	2.29	0.30	0.23
Fo507-I	723	1.09	1.16	1.78	2.19	0.29	0.25
Fo507-J	696	1.12	1.18	1.89	2.31	0.29	0.23

Nord (1982)								
Sample	Temp (K)	δ (mm/s)		Δ (mm/s)		X^{Fe}		Area M1/M2
		M1	M2	M1	M2	M1	M2	
H13	673	0.84	0.90	1.84	1.93	0.493	0.457	1.08

Nikitina (1982)						
Sample Range	Temp (K)	δ (mm/s)		Δ (mm/s)		% Fe in M2
		M1	M2	M1	M2	
$Fo_{0.06-0.15}$	550-603	1.14-1.18	1.20-1.25	2.01-2.18	2.34-2.50	M2 pref. up to 58%

Yupu (1982)								
Sample No.	Temp (K)	δ (mm/s)		Δ (mm/s)		Γ (mm/s)		M2/(M1+M2)
		M1	M2	M1	M2	left	right	
1	298	1.14		3.00		0.28	0.30	
	573	0.89	0.95	2.15	2.46	0.25		0.50
2	298	1.14		2.99		0.28	0.30	
	573	0.89	0.96	2.15	2.47	0.26		0.50
3	298	1.14		3.00		0.26	0.28	
	573	0.89	0.95	2.17	2.47	0.24		0.50
4	573	0.90	0.96	2.18	2.49	0.24		0.51
5	298	1.15		2.99		0.26	0.31	
	573	0.90	0.97	2.20	2.51	0.25		0.50
6	298	1.15		3.00		0.26	0.29	
	573	0.89	0.95	2.16	2.46	0.25		0.55
7	298	1.15		3.00		0.27	0.30	
8	573	0.89	0.97	2.18	2.49	0.25		0.55

9	573	0.89	0.97	2.19	2.49	0.24		0.51
10	573	0.88	0.96	2.16	2.46	0.25		0.55
11	573	0.88	0.95	2.14	2.45	0.24		0.54
12	573	0.90	0.97	2.21	2.50	0.24		0.53
13	298	1.15		3.03		0.28	0.28	
	473	0.97	1.04	2.46	2.72	0.25		0.53
	573	0.88	0.97	2.15	2.44	0.25		0.53
	753	0.76	0.83	1.80	2.12	0.24		0.48
	298	1.15		3.02		0.28		
14	298	1.15		2.84		0.27	0.34	
	573	0.89	0.95	2.01	2.45	0.28	0.28	0.49
15	300	1.28		2.94		0.57	0.57	
16	300	1.16		2.90				

Goncharenko (1995)

Microstructure types	T	δ (mm/s)		Δ (mm/s)		Areas M1/M2	Tot. area
		M1	M2	M1	M2		
Lath-type	RT	1.13±0.03	1.13±0.03	2.78±0.03	3.11±0.03	2.060	1.46
Porphyroclastic	RT	1.11±0.03	1.12±0.03	2.76±0.03	2.94±0.03	1.235	1.52
Porphyrolath-type	RT	1.14±0.03	1.12±0.03	2.80±0.03	3.01±0.03	2.658	1.22

Morozov (2005)

T (K)	δ (mm/s)		Δ (mm/s)		Γ (mm/s)		X_{Fe2+}		K_D	t_{ann} (days)
	M1	M2	M1	M2	M1	M2	M1	M2		
773	0.92	0.98	2.15	2.55	0.28	0.26	0.524	0.476	1.21	64
798	0.93	0.99	2.17	2.57	0.28	0.24	0.532	0.468	1.29	64
823	0.93	0.99	2.16	2.56	0.26	0.24	0.537	0.463	1.35	64
848	0.94	1.00	2.18	2.58	0.28	0.26	0.534	0.466	1.31	64
873	0.93	1.00	2.18	2.58	0.28	0.24	0.555	0.445	1.56	32
898	0.93	0.99	2.18	2.57	0.28	0.26	0.540	0.460	1.38	32
923	0.93	0.99	2.17	2.56	0.28	0.26	0.543	0.457	1.41	16
948	0.94	0.99	2.18	2.58	0.28	0.24	0.550	0.450	1.49	16
973	0.93	0.99	2.18	2.57	0.28	0.24	0.548	0.452	1.47	8
998	0.95	1.01	2.23	2.62	0.28	0.24	0.557	0.443	1.58	8
1023	0.94	1.00	2.19	2.58	0.28	0.24	0.549	0.451	1.48	2
1048	0.94	1.00	2.19	2.58	0.28	0.24	0.539	0.461	1.37	2
1073	0.94	1.00	2.19	2.59	0.28	0.24	0.574	0.426	1.82	2

$K_D = (X_{Fe}^{M1} * (1-X_{Fe}^{M2})) / (X_{Fe}^{M2} * (1-X_{Fe}^{M1}))$, $K_D > 1$ implies Fe^{2+} preference for M1 site, $t_{ann.}$ = annealing time

Chapter 3

Methods

This project started as the result of a conversation between Darby Dyar and Philip Bland over Olwyn Menzies' poster at the Lunar and Planetary Science Conference in 2001. In that poster the idea of correlating composition with quadrupole splitting in olivine was first suggested (Menzies, 2001). During Darby and Phil's discussion about the subject, Darby offered to run the synthetic samples of their original study at low temperature, as Phil and Olwyn lacked the Mössbauer apparatus to do so. This was the first project I was handed when I began working for Darby in the summer of 2004. A full investigation of these samples was performed in the much same manner described for the current study. Unfortunately, these original synthetic samples suffered from two problems: the samples were incompletely reacted, such that some of the original starting material remained; and some of the samples were slightly oxidized indicating poor control on oxygen fugacity during synthesis, so new samples were sought. All of the spectra for both studies can be viewed at: http://www.mtholyoke.edu/courses/mdyar/database/index.shtml?group=olivine. The original synthetic olivines are listed as "Menzies synthetic olivines" and the

samples used in this study are the "Lindsley synthetic olivines." The remainder of this thesis focuses on the Lindsley suite.

Sample Synthesis

Each sample was synthesized by the same method; all were supervised by Donald Lindsley and carried out in his laboratory at SUNY Stony Brook. A mixture of hematite and silicon was ground for 1-2 hours under ethanol. An iron sponge was then added and grinding continued for less than 1 hour. The product was wrapped in silver foil and placed in a silicon glass capsule. One end was sealed and the middle of the capsule was drawn out into a capillary, leaving the sample by the sealed end. An Fe getter was placed next to the open end of the capsule (Figure 3.1). The capsule was put into a vertical tube furnace at ~800°C (the Fe getter remained at ~600°C) for 10-20 min. The capsule was taken out of the furnace and sealed across the capillary (Figure 3.1). The completely sealed capsule section containing the sample was then placed in a horizontal tube furnace at ~920-940°C and cooked for 10 days.

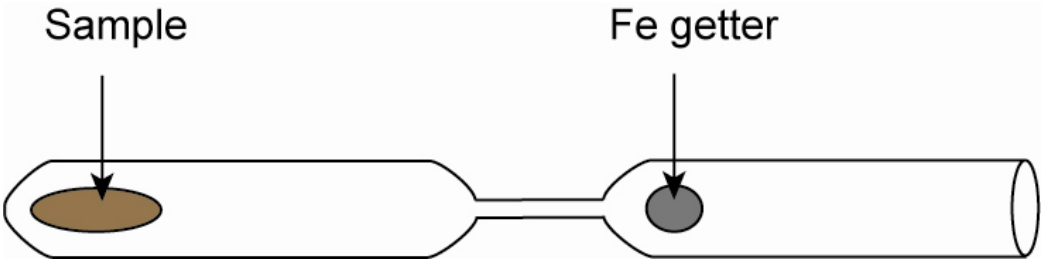

Figure 3.1; Schematic of tube in which sample is synthesized.

Sample Preparation

Synthetic olivine samples of 10-30 mg were ground using an Fe-free diamonite™ mortar and pestle under acetone to prevent oxidation. Samples were mixed with sugar and loaded into 34 mm diameter sample mounts. One side was sealed with an adhesive plastic cap and the other with thermal Kaptan tape. The sugar and grinding assure random orientation in the sample, and diluting with sugar ensures that thickness effects will be minimized, thus allowing, hopefully, for ideal thin absorber assumptions to be used in fitting.

Thickness Effects

It has been noted repeatedly that thickness corrections must be made on samples before doublet/sextet areas can be related to true abundance of the various Fe species (Margulies and Ehrman 1961, Ruby and Hicks 1962, Mørup and Both 1975, Rancourt 1989, Rancourt et al. 1993). Some workers have found that their samples require no thickness corrections at all (e.g., Bancroft and Brown, 1975). Thickness correction is not a straightforward process. First and foremost, the need must be determined. According to Grant (1995), the most straightforward way in which to do this is by comparison of Mössbauer data to XRD data. If the Mössbauer data are in conflict with the XRD data, thickness effects are usually the cause. Because there are no XRD data at this time to

compare with Mössbauer data, thickness calculations and corrections have not been made for the data in this project. In the continuing study of these samples, thickness effects will be given greater attention and corrections will be applied if necessary.

Mössbauer Spectroscopy of Samples

Variable temperature Mössbauer spectra were acquired on each sample under low He gas pressure at 15-17 different temperatures ranging from 13-293K. A source of 100-70 mCi ^{57}Co in Rh was used on a WEB Research Co. model W100 spectrometer equipped with a Janus closed-cycle He refrigerator. Run times ranged from 2-12 hours; results were calibrated against α-Fe foil. Typical count rates were between 500,000 and 900,000 non-resonant counts/hour.

Fitting Procedures

Paramagnetic spectra of antiferromagnetic minerals (unsplit spectra) were fit with Lorentzian line shapes using the method of Wivel and Mørup (1981). The program used was Mexfieldd, a component of a suite of programs created by Eddy De Grave and Toon van Alboom (Gent, Belgium). Mexfieldd uses Lorentzian line shapes to fit doublets with a fixed area ratio of 1:1 for the peaks. It solves the full Hamiltonian to determine single quadrupole splitting values (this

is distinguished from other programs where distributions are found for one or more parameters). Other variables are isomer shift and width. Best fits are determined by minimizing the chi squared (χ^2) value. See Grant (1995) for a full description of how this is done. Comparison fits for some of our spectra were performed using Disd3e_dd, a program that uses velocity approximations instead of solving full Hamiltonians to obtain values for isomer shift and quadrupole splitting. It searches for a distribution of quadrupole spitting values, rather than the single value sought in Mexdisdd. Quadrupole splitting distributions provide a non-Lorentzian lineshape (the lineshape is a sum of Voight lines) that has proved more correct for fitting certain types of Mössbauer spectra (Rancourt 1994). Magnetically split spectra were fit using Mexdisdd, which solves the full Hamiltonian to obtain values for quadrupole splitting, isomer shift, and magnetic field, but provides a distribution of values for the magnetic field parameter, similar to the quadrupole splitting distributions mentioned above.

Recoil-free Fraction and Characteristic Mössbauer Temperature

Recoil-free fractions were calculated using the program ISOMER, also developed by Eddy De Grave and Toon van Alboom. The program takes input values of temperature and isomer shift from the multi-temperature fits and calculates the recoil-free fraction across the available temperature range using the equation 2.14 (also displayed below).

$$\delta(T) = \delta_1 - \frac{9}{2}\frac{k_B T}{Mc}\left(\frac{T}{\Theta_M}\right)^3 \int_0^{\Theta_M/T} \frac{x^3 dx}{e^x - 1}$$

The method also calculates Θ_M, the characteristic Mössbauer temperature, which is a mathematical artifact of the Debye approximation used for the vibrational modes of the solid. The quantity Θ_M is useful in comparison with other Θ_M that have been calculated in the same way. It is a stepping-stone that allows calculation of other quantities such as recoil-free fraction and intrinsic isomer shift.

It was noted in Chapter 2 that the Debye model is not, in fact, a good approximation of a solid, but the approximation is widely enough used that comparison of values still provides insight. Plans have been made to begin work on an empirical method of calculating relative peak areas without the use of recoil-free fractions or the Debye approximation.

Chapter 4

Results

In order to explain the results of this study, the fitting procedure for a single sample will first be outlined, in order to elucidate results on all samples. Each spectrum was fit by the same procedure, so the choice of sample for this discussion is arbitrary, and a midrange composition of Fo_{40} was therefore chosen. The spectra that will be shown are the 293K spectra because if the M1 and M2 sites are distinguishable anywhere over the temperature range examined, the highest temperature spectrum is where they should be most distinct.

Before starting this discussion, a note must be made about comparisons between fits to different spectra. The typical statistical analysis of a fit is defined by the quantity χ^2, which takes into account the difference between the values calculated by the fitting program $Y_C(I)$ and the data points of the actual spectrum $Y_D(I)$. In symbols,

$$\chi^2 = \frac{1}{N-n}\sum_{I=1}^{N}\left(\frac{Y_C(I)-Y_D(I)}{\sqrt{Y_D(I)}}\right)^2,$$

where N is the number of points to be fitted, n is the number of fitting parameters, and $\sqrt{Y_D(I)}$ is the standard deviation of the experimental point I. This equation is applicable when the largest source of experimental uncertainty is counting

statistics (Ruby, 1973). Fits where $\chi^2 \approx 1$ are considered "good". However, caution must be used when examining χ^2 values for several reasons. First, because χ^2 is dependent on the standard deviation, it will decrease with increasing error bars. Therefore, poorer data quality may lead to χ^2 values closer to 1, and hence "better" fits. Second, the χ^2 values of fits to two different data sets have no meaning if they are compared, even if the data sets are acquired on the same sample (Dyar, 1984), because they have different baselines and counting statistics. Third, once an acceptable χ^2 range has been established for a given data set, two χ^2 values within that range can no longer be compared to ascertain which fit is "better" (Grant 1995). Fourth, counting statistics are not the only source of experimental error in Mössbauer spectra. In the following discussion, therefore, χ^2 values are used only as a general guide to the "goodness" of a fit.

The first fit of a spectrum is performed using only a single doublet. This is typically a valid place to start because the one doublet fit determines if additional doublets are needed (Figure 4.1). The fit for this spectrum using one doublet is inconsistent with the data in that the fit line does not reach far enough into the low velocity peak at -0.4 mm/s and reaches too far into the high velocity peak at 2.6 mm/s.

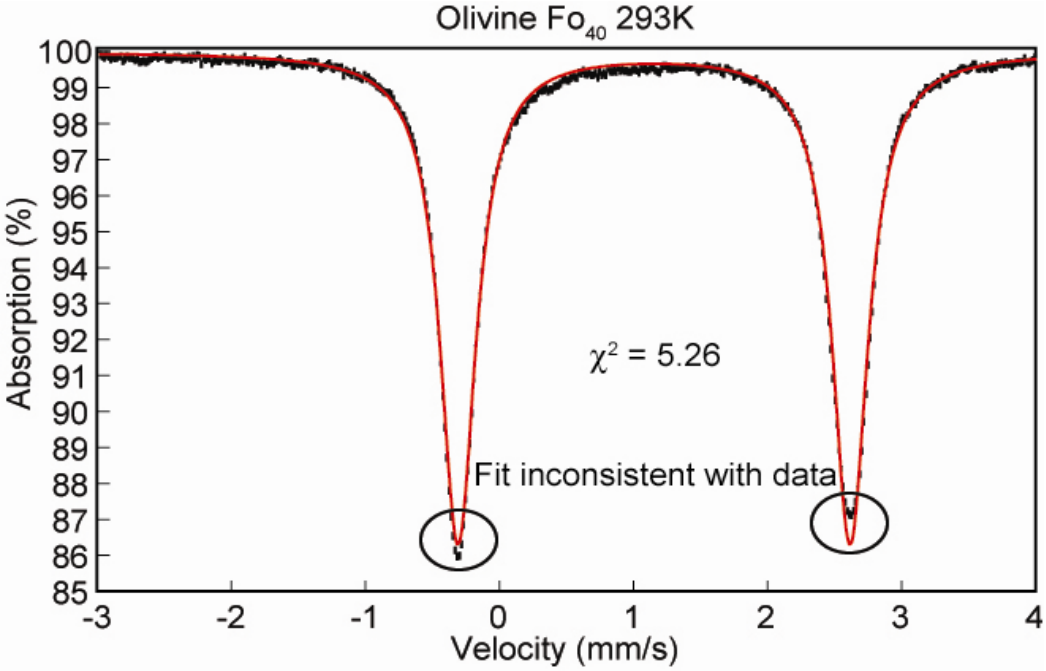

Figure 4.1; Olivine Fo_{40}, 293K, one doublet fit.

The fact that the peaks have unequal areas could mean more than one thing. There could be instrumental effects that broaden the higher velocity peak or thickness effects that similarly affect the areas (Vandenberghe 1994). To test these possibilities, all 293K spectra were fit using the program disd3e_dd that allows variation of peak areas. This program also uses quadrupole splitting distributions instead of purely Lorentzian lineshapes, so it permits analysis of each spectrum's adherence to the Lorentzian model as well as factors that cause area ratios to vary. If the inconsistencies of the one doublet fit were due to uneven areas from the above factors, then the inconsistencies should be resolved by allowing the areas of the two peaks to vary.

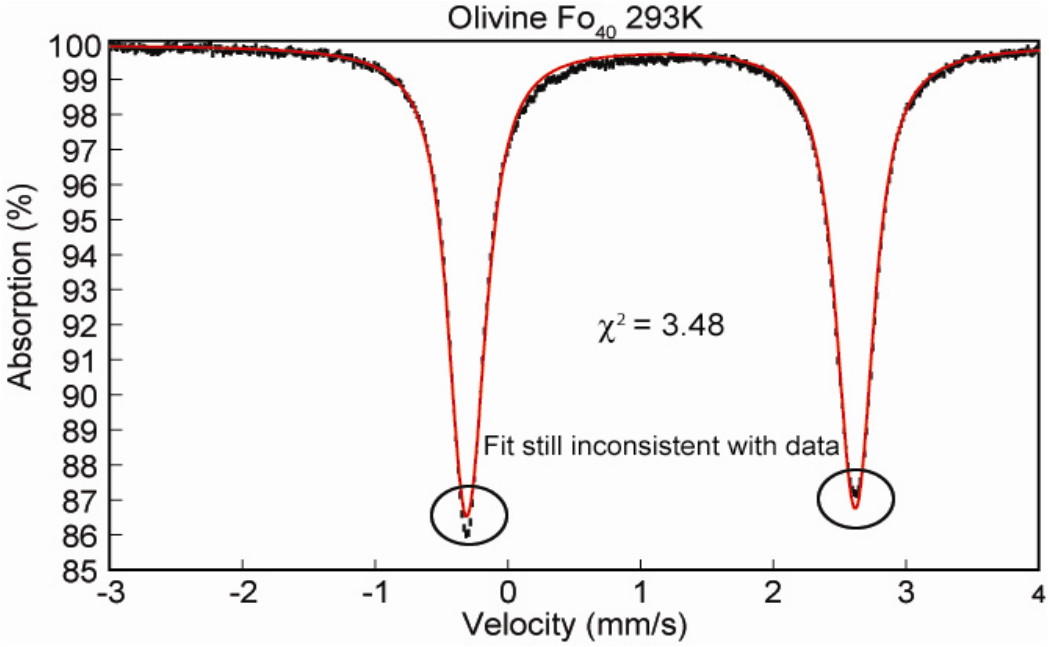

Figure 4.2; Olivine Fo_{40} 293K, A1/A2 allowed to vary. End area ratio A1/A2 = 1.017.

It is evident from Figure 4.2 that the inconsistencies between the fit and the data were not resolved by allowing the area ratios to vary and using quadrupole splitting distributions. Therefore, it seemed reasonable to use two doublets to fit the spectrum. This was done by pairing the doublet peaks in two ways: the 13_24 method and the 14_23 method. In the 13_24 method, peaks 1 and 3 (numbered from left to right, low to high velocity) are paired into the first doublet and peaks 2 and 4 are paired as the second doublet, i.e. the doublets are staggered. In the 14_23 method, 1 and 4 become one doublet and the peaks 2 and 3 correspond to the other, nesting inside the first. Below are the 293K Fo_{40} fits corresponding to these two fitting methods. For all fits, parameters were unconstrained.

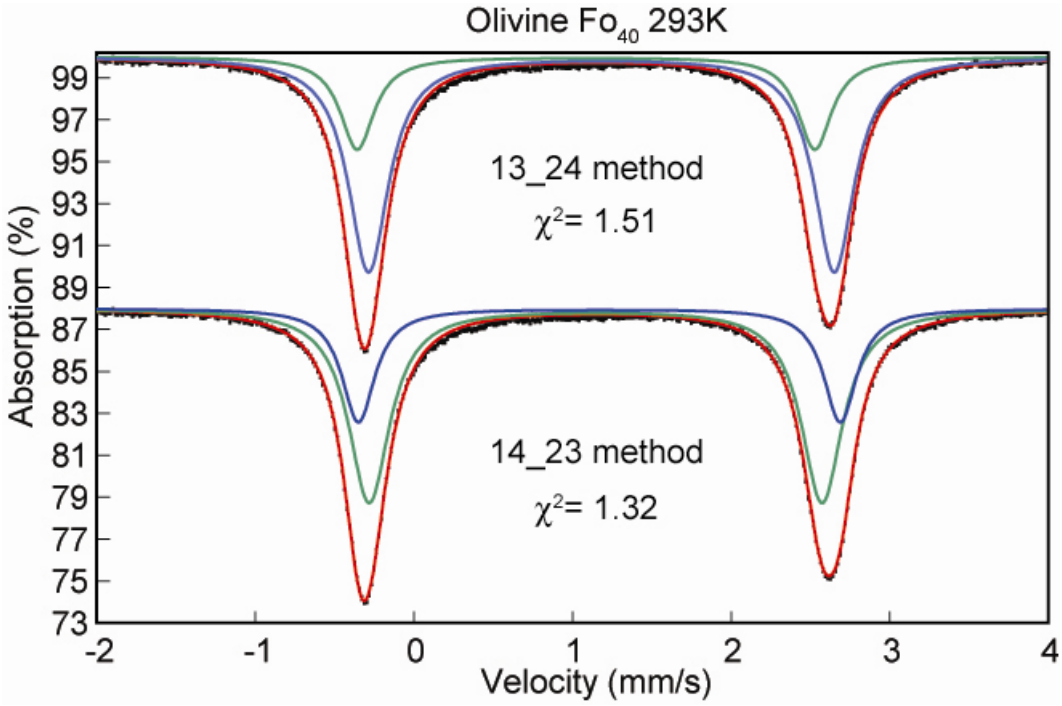

Figure 4.3; Comparison of two doublet fitting methods for Fo_{40}, 293K. The red line indicates the combined areas of the two doublets.

It is apparent from Figure 4.3 that a two doublet fit is a better approximation of the spectrum than the one doublet fit. The χ^2 values confirm this. For the two doublet fits, there is no way to say which model is better because both χ^2 values for the two fitting methods are within an acceptable range, arbitrarily defined for the purposes of this study as ±0.25 in the χ^2 value. The similarity between χ^2 values for the two fitting methods holds true for every spectrum, making it impossible to tell the results of the two fitting methods apart based on their χ^2 values alone.

To investigate the differences of these fitting methods further, full temperature series from 13-293K were examined. For any given sample,

sequential, well-resolved spectra at different temperatures should provide a smooth trend in both isomer shift (due to the systematic effect of the temperature-sensitive second order Doppler shift) and quadrupole splitting (from the temperature dependence of bonding behavior) with temperature. Below are the isomer shifts and quadrupole splittings plotted versus temperature for Fo_{40} using each fitting method. Note that the following graphical data (Figures 4.4 and 4.5) use fitting program results for isomer shift and quadrupole splitting that contain three decimal places, where the overall accuracy of the technique is ±0.02 mm/s (Dyar 1984). The graphical results, therefore, reflect the variation of parameters only as a function of numerical analysis of the data, rather than the overall error, which also includes heterogeneity of the sample.

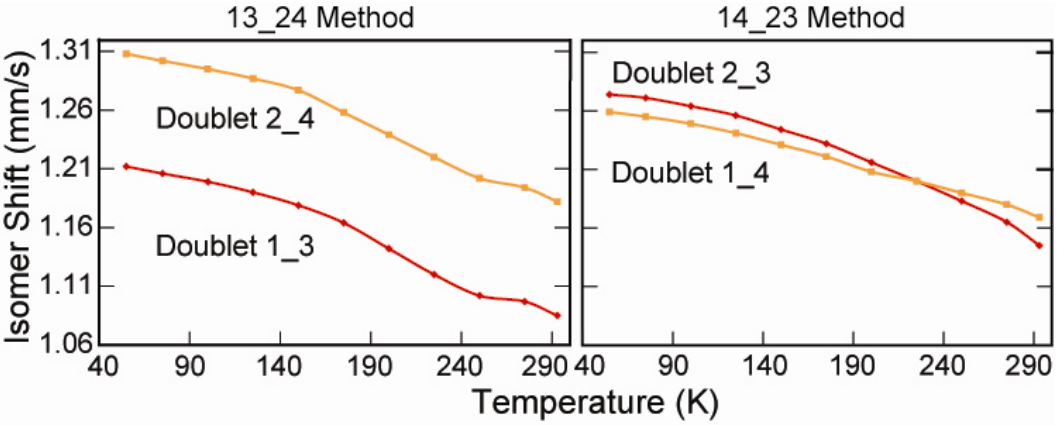

Figure 4.4; Isomer shift vs. temperature for Fo_{40} using the 13_24 fitting method (left) and the 14_23 fitting method (right).

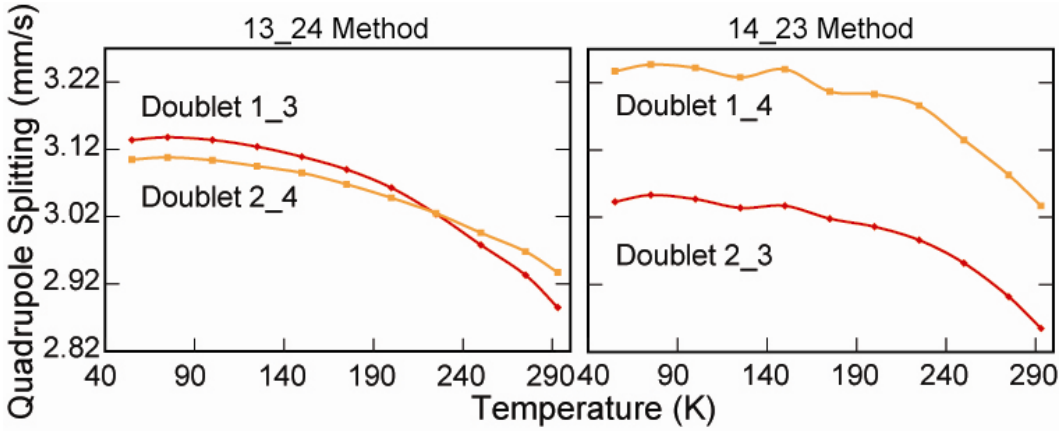

Figure 4.5; Quadrupole splitting vs. temperature for Fo_{40} using the 13_24 fitting method (left) and the 14_23 fitting method (right).

These figures show that for the 14_23 method, the isomer shift trend is smooth while the quadrupole splitting trend is irregular, and for the 13_24 method, the opposite is true. In addition, for the 14_23 method, the isomer shift curves cross at a certain temperature, while they do not cross for the 13_24 method. Again, the opposite is true for the quadrupole splitting curves. It seems that when the IS or QS values for the two curves are close together, then the IS vs. temperature and QS vs. temperature curves are smooth. This proved true for all compositions (Figure 4.6).

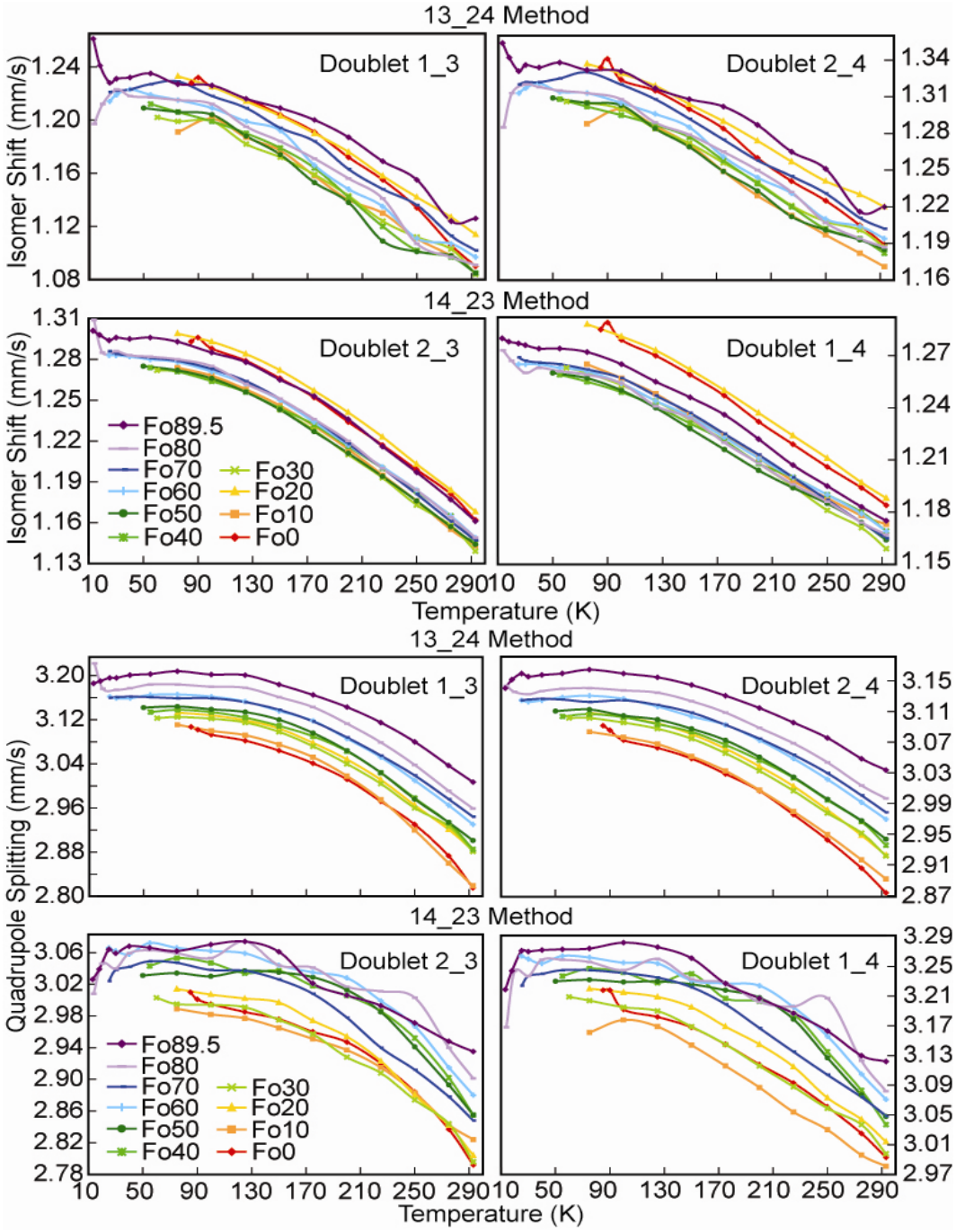

Figure 4.6; Isomer shift vs. temperature (top) and quadrupole splitting vs. temperature (bottom) using both fitting methods for all compositions. Color sequence is labeled in lower left plot.

Because both IS vs. temperature and QS vs. temperature curves should both ideally be smooth, this analysis does not shed any more light on the issue of which fitting method better represents the data. It was concluded at this point that the methods are indistinguishable without additional information from lower temperature (i.e., below 12K) split but magnetically ordered spectra and/or higher temperature spectra (above 293K) where the two doublets are more easily resolved (c.f., Shinno 1974). Pending upgrades to the laboratory at Mount Holyoke will facilitate acquisition of 4.2-12K spectra in the near future. High temperature data are currently being collected for us by Eddy De Grave at the University of Gent, Belgium.

Differentiating between these two fitting methods is of interest because it has been historically assumed (Goncharenko 1995, Morozov 2005, Nikitina 1982, Nord 1982, Shinno 1974, Yupu 1982) that each doublet is representative of iron in a particular octahedrally coordinated site (M1 or M2) in the olivine structure. Typically, doublet 2_3 from the 14_23 fitting method has been assigned to the smaller, more distorted M1 site. Brown (1980) concluded in a review paper on olivine that Fe shows a slight preference for the M1 site. If the doublets are representative of coordination sites, and there is slight ordering, then there should be some sort of systematic change in the Fe site occupancies, as represented by doublet areas, as the Fe/Mg ratio changes. To examine this possibility, two approaches were taken, one to test for partial ordering and one to test for complete ordering:

1. All spectra were fit without any constraints (the data sets displayed in Figures 4.6). The areas of the two doublets were examined for systematic trends that could be related to cation ordering. In other words, if one doublet is assigned to M1 and the other to M2, and if Fe^{2+} preferentially occupies one or the other of these two sites, then a systematic change in the areas of the doublets assigned to M1 and M2 should be observed as the composition changes. It was found that the ratios of the "M1" and "M2" doublet areas could not be associated with any systematic changes in composition. For example, Fe^{2+} completely fills both the M1 and the M2 sites in pure fayalite ($^{M1}Fe^{M2}FeSiO_4$). The sites exist in a 1:1 ratio. Thus, if the "M1"and M2" doublets truly represent Fe in those sites, then the doublets should have areas in the ratio of 1:1. Instead, in these fits, an average 70:30 area ratio was found for Fo_0.
2. All 270K and 293K spectra were fit with fixed area ratios to simulate ratios that would represent complete ordering (for example, 50:50 doublet areas for the Fo_0 spectra and 100:0 ratios for the Fo_{50} spectra). This was done both forcing Fe into the "M1" doublet and the "M2" doublet in a ratio appropriate to each composition, and using both fitting methods. These fits had greatly elevated χ^2 values and fit inconsistencies. For example, χ^2 values Fo^{70} at 293K went from 1.90

and 1.84 for 13_24 and 14_23 fitting methods respectively to 16.65 for a fully ordered configuration (where all Fe is in either the M1 or M2 site).

These tests showed that the two doublets cannot, at these temperatures, be consistently assigned to any ordered distribution between the M1 and M2 sites. Because two doublets are resolved, however, it seemed necessary to find a way to catalogue the changes in these two doublets with varying temperature and composition. Therefore, all spectra were fit with the two doublets where the doublets are constrained to have equal widths, although that width could vary. The results of those fits are listed in graphical (Figure 4.7) and tabular (Table 4.1) form below.

Figures 4.6 and 4.7 show that line width affects both isomer shift and quadrupole splitting for doublets with a high degree of overlap. Use of width constraints leads to a smoother, more regular curve for both isomer shift and quadrupole splitting vs. temperature. Therefore, due to the degree of overlap of the doublets, neither doublet area nor smoothness of isomer shift and quadrupole splitting vs. temperature trends can be used as diagnostic criteria to confirm which fitting method is more “real”.

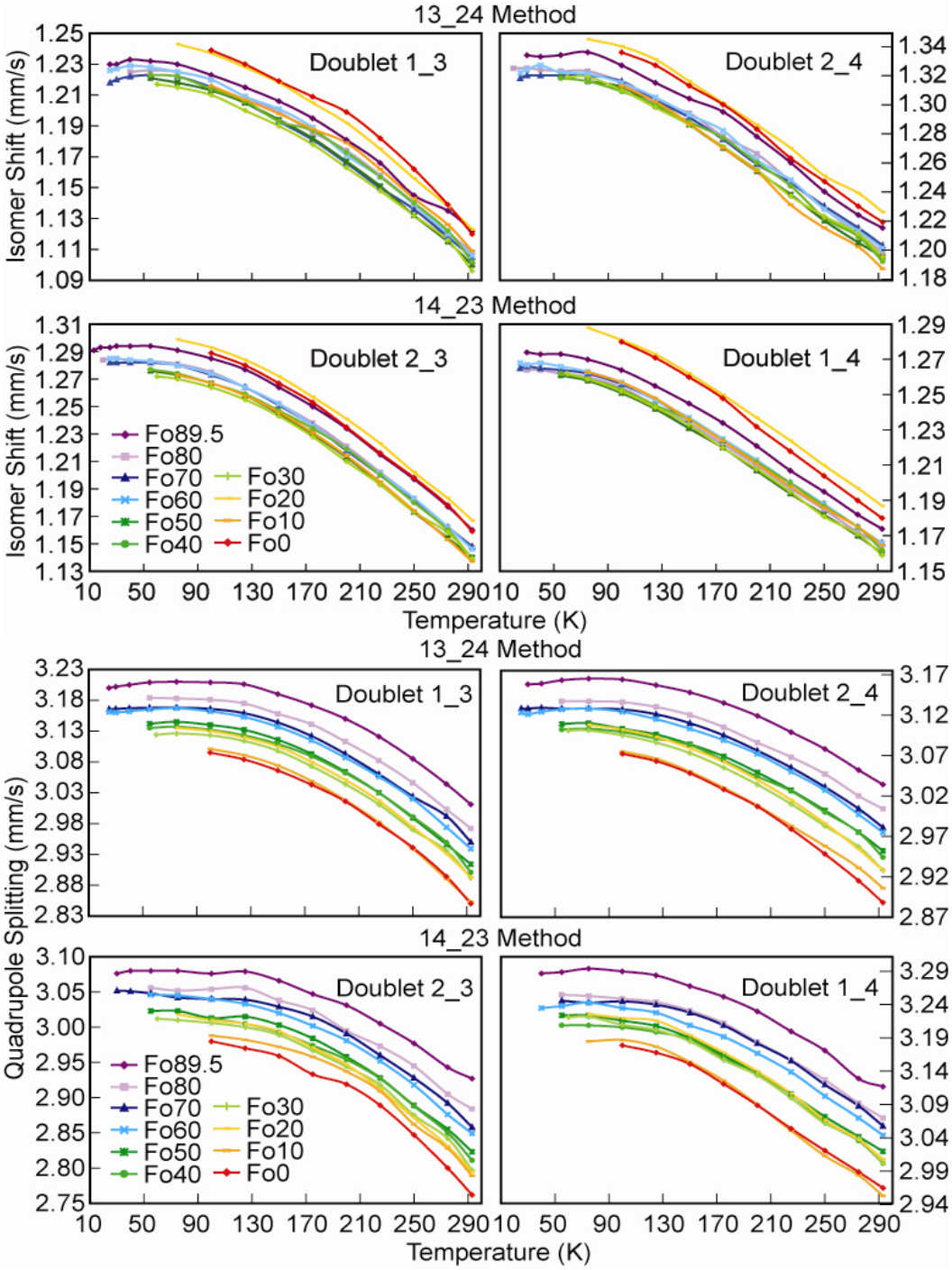

Figure 4.7; Isomer shift vs. temperature (top) and quadrupole splitting vs. temperature (bottom) using both fitting methods, applying correlation on the doublet widths, for all compositions. Color sequence is labeled in lower left plot.

Table 4.1; Isomer shift and quadrupole splitting values for 13_24 and 14_23 fitting method. Isomer shift and quadrupole splitting are in mm/s. Isomer shift is relative to α-Fe foil. Errors on isomer shift and quadrupole splitting are ± 0.02mm/s. The differences in temperature progressions for certain compositions are due to procedural variations in those runs due to time constraints or acquisition of additional information for those compositions, such as magnetic ordering temperature.

Isomer Shifts for Doublet 1_3, 13_24 Fitting Method (mm/s)										
T(K)	**$Fo_{89.5}$**	**Fo_{80}**	**Fo_{70}**	**Fo_{60}**	**Fo_{50}**	**Fo_{40}**	**Fo_{30}**	**Fo_{20}**	**Fo_{10}**	**Fo_{0}**
293	1.12	1.11	1.11	1.11	1.10	1.10	1.10	1.12	1.11	1.12
275	1.14	1.12	1.12	1.12	1.12	1.12	1.12	1.14	1.13	1.14
250	1.15	1.14	1.14	1.14	1.13	1.14	1.13	1.16	1.14	1.16
225	1.17	1.16	1.15	1.16	1.15	1.16	1.15	1.18	1.16	1.18
200	1.18	1.17	1.17	1.17	1.17	1.17	1.16	1.19	1.18	1.20
175	1.20	1.19	1.18	1.19	1.18	1.19	1.18	1.21	1.19	1.21
150	1.21	1.20	1.19	1.20	1.19	1.19	1.19	1.22	1.20	1.22
125	1.22	1.21	1.21	1.21	1.21	1.19	1.20	1.23	1.21	1.23
100	1.22	1.22	1.22	1.22	1.21	1.21	1.21	1.24	1.22	1.24
75	1.23	1.23	1.22	1.23	1.22	1.21	1.22	1.24	1.23	
60							1.22			
55	1.23	1.23	1.22	1.23		1.22				
50					1.22					
40	1.23	1.23	1.22	1.23	1.24	1.22				
30	1.23	1.23	1.22	1.23						
25	1.23		1.22	1.23						
20		1.23								
18	1.23									
13.8		1.24								
13.1	1.24									
Isomer Shifts for Doublet 2_4, 13_24 Fitting Method (mm/s)										
T(K)	**$Fo_{89.5}$**	**Fo_{80}**	**Fo_{70}**	**Fo_{60}**	**Fo_{50}**	**Fo_{40}**	**Fo_{30}**	**Fo_{20}**	**Fo_{10}**	**Fo_{0}**
293	1.22	1.20	1.20	1.20	1.20	1.19	1.20	1.23	1.19	1.22
275	1.23	1.21	1.22	1.21	1.21	1.21	1.21	1.24	1.20	1.23
250	1.24	1.22	1.23	1.23	1.22	1.22	1.22	1.25	1.22	1.25
225	1.26	1.25	1.25	1.25	1.24	1.25	1.24	1.27	1.23	1.26
200	1.28	1.27	1.26	1.26	1.26	1.26	1.26	1.29	1.26	1.28
175	1.30	1.28	1.28	1.28	1.27	1.28	1.27	1.30	1.27	1.30
150	1.31	1.30	1.29	1.29	1.29	1.29	1.29	1.32	1.29	1.31
125	1.32	1.30	1.30	1.31	1.30	1.30	1.30	1.33	1.30	1.33
100	1.33	1.32	1.32	1.32	1.31	1.31	1.31	1.34	1.31	1.34
75	1.34	1.32	1.32	1.32	1.32	1.32	1.32	1.35	1.31	
60							1.32			
55	1.34	1.32	1.32	1.32		1.32				
50					1.32					
40	1.33	1.33	1.32	1.33	1.30					
30	1.34	1.32	1.32	1.33						
25	1.33		1.32	1.32						
20		1.32								
18	1.33		1.32							
13.8		1.31								

13.1	1.33									
Isomer Shifts for Doublet 1_4, 14_23 Fitting Method (mm/s)										
T(K)	**$Fo_{89.5}$**	**Fo_{80}**	**Fo_{70}**	**Fo_{60}**	**Fo_{50}**	**Fo_{40}**	**Fo_{30}**	**Fo_{20}**	**Fo_{10}**	**Fo_{0}**
293	1.17	1.17	1.17	1.17	1.16	1.16	1.16	1.19	1.17	1.18
275	1.18	1.17	1.18	1.18	1.17	1.18	1.17	1.20	1.18	1.19
250	1.20	1.19	1.19	1.19	1.18	1.19	1.18	1.21	1.19	1.20
225	1.21	1.20	1.20	1.20	1.19	1.20	1.20	1.22	1.20	1.22
200	1.22	1.21	1.21	1.21	1.21	1.21	1.21	1.24	1.21	1.23
175	1.23	1.22	1.22	1.23	1.22	1.22	1.22	1.25	1.22	1.25
150	1.25	1.23	1.24	1.24	1.23	1.24	1.23	1.26	1.24	1.26
125	1.26	1.24	1.25	1.25	1.24	1.24	1.24	1.27	1.25	1.27
100	1.26	1.25	1.26	1.26	1.25	1.25	1.25	1.28	1.26	1.28
75	1.27	1.26	1.26	1.26	1.26	1.26	1.26	1.29	1.26	
60							1.26			
55	1.27	1.26	1.26	1.27		1.26				
50					1.26					
40	1.27	1.26	1.27	1.27	1.26					
30	1.27	1.26	1.27	1.27						
25	1.28		1.27	1.27						
20		1.27								
18	1.27									
13.8		1.26								
13.1	1.28									
Isomer Shifts for Doublet 2_3, 14_23 Fitting Method (mm/s)										
T(K)	**$Fo_{89.5}$**	**Fo_{80}**	**Fo_{70}**	**Fo_{60}**	**Fo_{50}**	**Fo_{40}**	**Fo_{30}**	**Fo_{20}**	**Fo_{10}**	**Fo_{0}**
293	1.16	1.15	1.15	1.15	1.14	1.14	1.14	1.17	1.14	1.16
275	1.18	1.16	1.16	1.16	1.15	1.16	1.16	1.18	1.15	1.18
250	1.20	1.18	1.18	1.18	1.17	1.18	1.17	1.20	1.17	1.20
225	1.22	1.20	1.20	1.20	1.19	1.20	1.19	1.22	1.20	1.22
200	1.23	1.22	1.22	1.22	1.21	1.22	1.21	1.24	1.21	1.24
175	1.25	1.24	1.24	1.24	1.23	1.23	1.23	1.26	1.23	1.25
150	1.26	1.25	1.25	1.25	1.25	1.25	1.24	1.27	1.25	1.27
125	1.28	1.26	1.26	1.26	1.26	1.26	1.26	1.28	1.26	1.28
100	1.29	1.28	1.27	1.27	1.27	1.27	1.26	1.29	1.27	1.29
75	1.29	1.28	1.28	1.28	1.27	1.27	1.27	1.30	1.27	
60							1.27			
55	1.29	1.28	1.28	1.28		1.28				
50					1.28					
40	1.29	1.28	1.28	1.28	1.28					
30	1.29	1.29	1.28	1.29						
25	1.29		1.28	1.29						
20		1.28								
18	1.29									
13.8		1.29								
13.1	1.29									
Quadrupole Splitting for Doublet 1_3, 13_24 Fitting Method (mm/s)										
T(K)	**$Fo_{89.5}$**	**Fo_{80}**	**Fo_{70}**	**Fo_{60}**	**Fo_{50}**	**Fo_{40}**	**Fo_{30}**	**Fo_{20}**	**Fo_{10}**	**Fo_{0}**
293	3.01	2.97	2.95	2.93	2.91	2.90	2.89	2.89	2.85	2.85
275	3.04	3.00	2.99	2.97	2.94	2.94	2.93	2.93	2.89	2.89
250	3.08	3.04	3.02	3.02	2.98	2.99	2.97	2.97	2.93	2.94

225	3.12	3.08	3.06	3.05	3.03	3.03	3.01	3.01	2.98	2.97
200	3.15	3.11	3.07	3.08	3.06	3.06	3.04	3.05	3.01	3.01
175	3.17	3.14	3.12	3.11	3.09	3.08	3.07	3.08	3.04	3.04
150	3.19	3.15	3.14	3.13	3.11	3.10	3.09	3.10	3.07	3.06
125	3.20	3.17	3.15	3.15	3.13	3.12	3.11	3.12	3.09	3.08
100	3.20	3.18	3.16	3.16	3.13	3.13	3.12	3.13	3.10	3.09
75	3.21	3.18	3.16	3.16	3.14	3.13	3.12	3.13	3.10	
60							3.12			
55	3.20	3.18	3.16	3.16		3.13				
50					3.14					
40	3.20	3.17	3.16	3.16	3.14					
30	3.20	3.17	3.16	3.16						
25	3.20		3.16	3.16						
20		3.17								
18	3.19									
13.8		3.18								
13.1	3.19									
Quadrupole Splitting for Doublet 2_4, 13_24 Fitting Method (mm/s)										
T(K)	**$Fo_{89.5}$**	**Fo_{80}**	**Fo_{70}**	**Fo_{60}**	**Fo_{50}**	**Fo_{40}**	**Fo_{30}**	**Fo_{20}**	**Fo_{10}**	**Fo_{0}**
293	3.03	3.00	2.98	2.98	2.95	2.94	2.93	2.93	2.91	2.89
275	3.05	3.02	3.00	3.00	2.98	2.98	2.96	2.95	2.93	2.92
250	3.08	3.05	3.03	3.03	3.00	3.00	2.98	2.99	2.96	2.95
225	3.10	3.07	3.06	3.05	3.03	3.03	3.01	3.02	2.98	2.98
200	3.12	3.09	3.08	3.07	3.05	3.04	3.03	3.04	3.01	3.01
175	3.14	3.11	3.10	3.09	3.07	3.06	3.06	3.06	3.03	3.03
150	3.15	3.12	3.11	3.10	3.08	3.08	3.07	3.08	3.05	3.05
125	3.16	3.13	3.12	3.12	3.10	3.09	3.09	3.09	3.07	3.06
100	3.16	3.14	3.13	3.12	3.10	3.10	3.10	3.10	3.08	3.07
75	3.17	3.14	3.13	3.13	3.11	3.10	3.10	3.11	3.08	
60							3.10			
55	3.16	3.14	3.13	3.13		3.10				
50					3.11					
40	3.16	3.14	3.13	3.12	3.11					
30	3.16	3.13	3.13	3.12						
25	3.16		3.13	3.12						
20		3.13								
18	3.16									
13.8		3.13								
13.1	3.16									
Quadrupole Splitting for Doublet 1_4, 14_23 Fitting Method (mm/s)										
T(K)	**$Fo_{89.5}$**	**Fo_{80}**	**Fo_{70}**	**Fo_{60}**	**Fo_{50}**	**Fo_{40}**	**Fo_{30}**	**Fo_{20}**	**Fo_{10}**	**Fo_{0}**
293	3.12	3.07	3.06	3.04	3.02	3.00	3.00	3.01	2.95	2.96
275	3.13	3.09	3.09	3.07	3.04	3.03	3.04	3.04	2.98	2.99
250	3.17	3.13	3.12	3.10	3.07	3.06	3.06	3.07	3.01	3.02
225	3.20	3.16	3.15	3.14	3.10	3.10	3.10	3.11	3.05	3.05
200	3.23	3.18	3.18	3.17	3.14	3.13	3.13	3.14	3.09	3.09
175	3.25	3.21	3.21	3.19	3.16	3.16	3.16	3.17	3.12	3.12
150	3.27	3.23	3.23	3.21	3.19	3.19	3.18	3.19	3.15	3.15
125	3.28	3.24	3.24	3.23	3.21	3.20	3.20	3.21	3.18	3.17
100	3.29	3.25	3.24	3.23	3.21	3.20	3.21	3.22	3.19	3.18

75	3.29	3.25	3.24	3.24	3.22	3.21	3.22	3.22	3.18	
60							3.22			
55	3.29	3.25	3.24	3.24		3.21				
50					3.22					
40	3.29	3.25	3.25	3.23	3.19					
30	3.29	3.25	3.26	3.24						
25	3.29		3.26	3.24						
20		3.25								
18	3.28									
13.8		3.23								
13.1	3.28									
Quadrupole Splitting for Doublet 2_3, 14_23 Fitting Method (mm/s)										
T(K)	**$Fo_{89.5}$**	**Fo_{80}**	**Fo_{70}**	**Fo_{60}**	**Fo_{50}**	**Fo_{40}**	**Fo_{30}**	**Fo_{20}**	**Fo_{10}**	**Fo_{0}**
293	2.92	2.89	2.86	2.85	2.82	2.81	2.80	2.80	2.79	2.76
275	2.94	2.91	2.89	2.88	2.86	2.85	2.84	2.83	2.83	2.80
250	2.98	2.95	2.93	2.92	2.89	2.89	2.88	2.87	2.6	2.85
225	3.01	2.97	2.96	2.95	2.93	2.93	2.92	2.91	2.91	2.89
200	3.03	3.00	2.99	2.98	2.96	2.95	2.94	2.95	2.94	2.92
175	3.05	3.02	3.02	3.00	2.98	2.97	2.97	2.97	2.96	2.93
150	3.07	3.04	3.03	3.02	3.00	2.99	2.99	2.99	2.97	2.96
125	3.08	3.06	3.04	3.03	3.02	3.01	3.00	3.01	2.98	2.97
100	3.08	3.05	3.04	3.04	3.01	3.01	3.01	3.01	2.99	2.98
75	3.08	3.05	3.04	3.05	3.02	3.02	3.01	3.02	3.01	
60							3.01			
55	3.08	3.06	3.05	3.05		3.01				
50					3.02					
40	3.08	3.05	3.05	3.04	3.06					
30	3.08	3.05	3.05	3.04						
25	3.08		3.06	3.05						
20		3.06								
18	3.08									
13.8		3.09								
13.1	3.10									

Two doublets are essential for successful modeling of high resolution data. For many Mössbauer applications, however, such resolution is not possible. For example, rock spectra where olivine is Mg rich or extraterrestrial spectra where count rates are limited. For comparison with such cases, a comprehensive set of fits using only one doublet was obtained over the composition and temperature range. Because each doublet in the two doublet fits seems to be a hybrid representation of the M1 and M2 sites, the additional benefit of a one doublet

study is that certain trends that may have been masked by the variations between the doublets become clear. Essentially, the M1 and M2 site parameters are completely averaged and the overall energy of the peaks as a whole can be investigated. Graphical (Figure 4.8) and numerical (Table 4.2) results of the one doublet study are below.

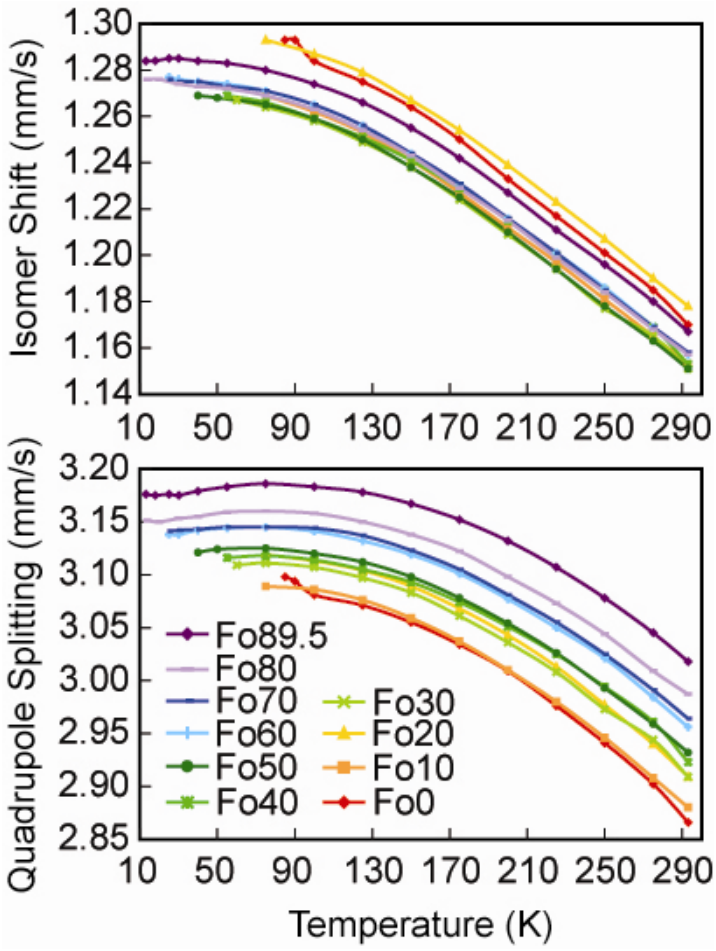

Figure 4.8; Isomer shift vs. temperature (top) and quadrupole splitting vs. temperature (bottom) for one doublet fits on all compositions. Color scheme is labeled in lower plot.

Table 4.2; Isomer shift and quadrupole splitting values for one doublet fitting method. Isomer shift and quadrupole splitting are in mm/s. Isomer shift is relative to α-Fe foil. Errors on isomer shift and quadrupole splitting are ± 0.02mm/s. The differences in temperature progressions for certain compositions are due to procedural variations in those runs due to time constraints or acquisition of additional information for those compositions, such as magnetic ordering temperature.

Isomer shifts for one doublet fits on Lindsley synthetic samples (mm/s)										
T(K)	**$Fo_{89.5}$**	**Fo_{80}**	**Fo_{70}**	**Fo_{60}**	**Fo_{50}**	**Fo_{40}**	**Fo_{30}**	**Fo_{20}**	**Fo_{10}**	**Fo_{0}**
293	1.17	1.16	1.16	1.16	1.15	1.15	1.15	1.18	1.15	1.17
275	1.18	1.17	1.17	1.17	1.16	1.17	1.17	1.19	1.17	1.19
250	1.20	1.18	1.19	1.19	1.18	1.19	1.18	1.21	1.18	1.20
225	1.21	1.20	1.20	1.20	1.19	1.20	1.19	1.22	1.20	1.22
200	1.23	1.22	1.22	1.22	1.21	1.22	1.21	1.24	1.21	1.23
175	1.24	1.23	1.23	1.23	1.23	1.23	1.22	1.25	1.23	1.25
150	1.26	1.24	1.24	1.24	1.24	1.24	1.24	1.27	1.24	1.26
125	1.27	1.25	1.26	1.26	1.25	1.25	1.25	1.28	1.25	1.28
100	1.27	1.26	1.27	1.27	1.26	1.26	1.26	1.29	1.26	1.29
75	1.28	1.27	1.27	1.27	1.27	1.27	1.26	1.29	1.27	
60							1.26			
55	1.28	1.27	1.27	1.27		1.27				
50					1.27					
40	1.28	1.27	1.28	1.28	1.27					
30	1.29	1.27	1.28	1.28						
25	1.29		1.28	1.28						
20		1.28								
18	1.28									
13.8		1.28								
13.1	1.28									
Quadrupole splitting for one doublet fits on Lindsley synthetic samples (mm/s)										
T(K)	**$Fo_{89.5}$**	**Fo_{80}**	**Fo_{70}**	**Fo_{60}**	**Fo_{50}**	**Fo_{40}**	**Fo_{30}**	**Fo_{20}**	**Fo_{10}**	**Fo_{0}**
293	3.02	2.99	2.96	2.96	2.93	2.93	2.91	2.91	2.89	2.87
275	3.05	3.01	2.99	2.98	2.96	2.96	2.94	2.94	2.91	2.90
250	3.08	3.04	3.03	3.02	2.99	2.99	2.97	2.98	2.95	2.94
225	3.11	3.07	3.06	3.05	3.03	3.03	3.01	3.01	2.98	2.98
200	3.13	3.10	3.08	3.08	3.05	3.05	3.04	3.04	3.01	3.01
175	3.15	3.12	3.11	3.10	3.08	3.07	3.06	3.07	3.03	3.03
150	3.17	3.14	3.12	3.12	3.10	3.09	3.08	3.09	3.06	3.06
125	3.18	3.15	3.14	3.13	3.11	3.11	3.10	3.10	3.08	3.07
100	3.18	3.16	3.14	3.14	3.12	3.11	3.11	3.11	3.09	3.08
75	3.19	3.16	3.15	3.15	3.13	3.12	3.11	3.12	3.09	
60							3.11			
55	3.18	3.16	3.15	3.14		3.12				
50					3.12					
40	3.18	3.16	3.14	3.14	3.12					
30	3.18	3.15	3.14	3.14						
25	3.18		3.14	3.14						
20		3.15								
18	3.18									
13.8		3.15								

13.1	3.18									

From the isomer shift and temperature data, recoil-free fractions were calculated. These values were calculated both for the two doublet, correlated width fits, and for the one doublet fits. Because the purpose of the recoil-free fraction value is to correct for area ratios in a mixed mineral spectrum, the one doublet recoil-free fraction values should prove of greater use in olivine fits where resolution of more than one doublet is impractical. These data are shown in Figures 4.9, 4.10 and 4.11 and in Tables 4.3 and 4.4. The recoil-free fraction values in the table are given for different temperatures depending upon the olivine composition, because the program used calculates recoil-free fraction values using a fixed step size starting at the lowest temperature data.

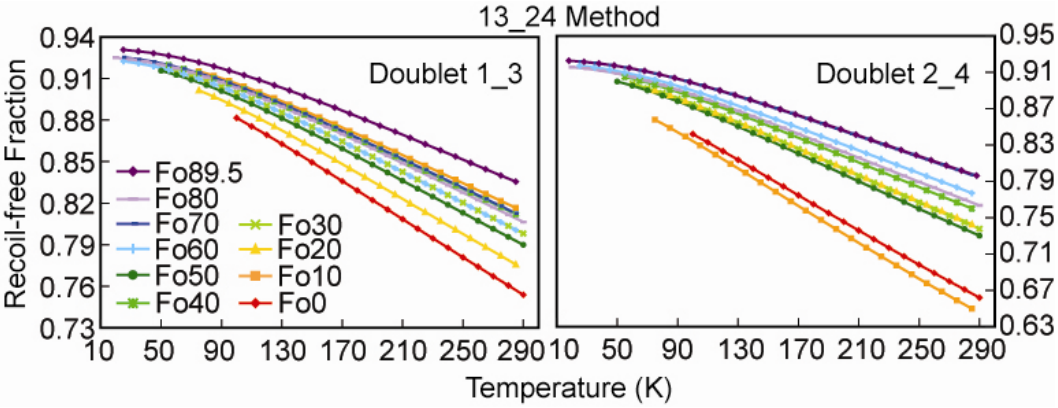

Figure 4.9; Recoil-free fraction vs. temperature plots for two doublet, correlated width fits using 13_24 fitting method. The color scheme is labeled in the lower left plot.

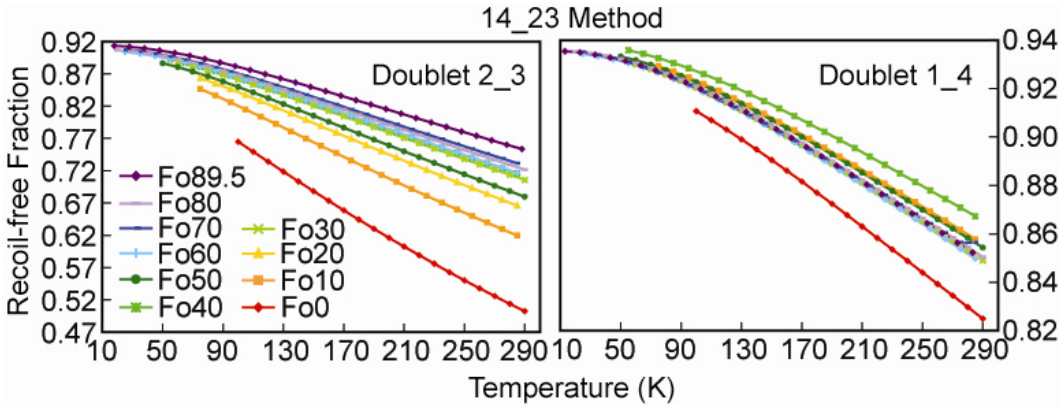

Figure 4.10; Recoil-free fraction vs. temperature plots for two doublet, correlated width fits using 14_23 fitting method. The color scheme is labeled in the lower left plot.

Table 4.3; Recoil-free fractions across the 13K-293K temperature range for two doublet fits using both fitting methods. The recoil-free fraction, being a ratio, is dimensionless. The gaps in the tables are an artifact of the fixed step size of the program calculating the recoil-free fractions.

Recoil-free Fractions for Doublet 1_3, 13_24 Method										
T(K)	**$Fo_{89.5}$**	**Fo_{80}**	**Fo_{70}**	**Fo_{60}**	**Fo_{50}**	**Fo_{40}**	**Fo_{30}**	**Fo_{20}**	**Fo_{10}**	**Fo_{0}**
290		0.806			0.790		0.798			0.754
285	0.835		0.813	0.801		0.812		0.776	0.817	
280		0.812			0.796		0.804			0.760
275	0.840		0.818	0.803		0.817		0.782	0.822	
270		0.817			0.801		0.809			0.767
265	0.845		0.823	0.812		0.822		0.788	0.827	
260		0.822			0.807		0.815			0.774
255	0.849		0.828	0.817		0.828		0.795	0.832	
250		0.828			0.813		0.820			0.781
245	0.854		0.834	0.823		0.833		0.801	0.837	
240		0.833			0.819		0.826			0.788
235	0.858		0.839	0.829		0.838		0.807	0.842	
230		0.838			0.825		0.831			0.795
225	0.862		0.844	0.834		0.843		0.814	0.847	
220		0.844			0.831		0.837			0.802
215	0.867		0.849	0.840		0.849		0.820	0.852	
210		0.849			0.836		0.843			0.808
205	0.872		0.854	0.845		0.854		0.826	0.857	
200		0.854			0.842		0.848			0.815
195	0.876		0.860	0.851		0.859		0.832	0.862	
190		0.859			0.848		0.854			0.822
185	0.880		0.865	0.856		0.864		0.839	0.867	
180		0.865			0.854		0.859			0.829
175	0.885		0.870	0.861		0.869		0.845	0.872	
170		0.870			0.859		0.865			0.836
165	0.889		0.875	0.867		0.874		0.851	0.877	
160		0.875			0.865		0.870			0.843

155	0.893		0.879	0.872		0.879		0.858	0.882	
150		0.880			0.871		0.875			0.850
145	0.897		0.884	0.878		0.884		0.864	0.887	
140		0.885			0.876		0.880			0.856
135	0.901		0.889	0.883		0.889		0.870	0.891	
130		0.890			0.881		0.886			0.863
125	0.905		0.893	0.888		0.894		0.875	0.896	
120		0.894			0.887		0.890			0.869
115	0.909		0.898	0.893		0.898		0.881	0.900	
110		0.899			0.892		0.895			0.876
105	0.912		0.903	0.897		0.902		0.887	0.904	
100		0.903			0.896		0.900			0.881
95	0.916		0.907	0.902		0.906		0.892	0.908	
90		0.907			0.901		0.904			
85	0.919		0.910	0.906		0.910		0.897	0.912	
80		0.911			0.905		0.908			
75	0.922		0.914	0.910		0.914		0.901	0.915	
70		0.914			0.909		0.912			
65	0.924		0.917	0.913		0.917				
60		0.917			0.913		0.915			
55	0.926		0.920	0.906		0.920				
50		0.920			0.916					
45	0.928		0.922	0.919						
40		0.922								
35	0.930		0.924	0.921						
30		0.924								
25	0.931		0.925	0.922						
20		0.925								
Recoil-free Fractions for Doublet 2_4, 13_24 Method										
T(K)	**$Fo_{89.5}$**	**Fo_{80}**	**Fo_{70}**	**Fo_{60}**	**Fo_{50}**	**Fo_{40}**	**Fo_{30}**	**Fo_{20}**	**Fo_{10}**	**Fo_{0}**
290		0.763			0.730		0.738			0.662
288	0.796									
285			0.797	0.777		0.760		0.743	0.650	
280		0.770			0.738		0.745			0.671
278	0.802									
275			0.803	0.783		0.767		0.750	0.659	
270		0.776			0.745		0.752			0.680
268	0.808									
265			0.808	0.790		0.774		0.757	0.669	
260		0.783			0.752		0.759			0.689
258	0.813									
255			0.814	0.796		0.780		0.764	0.678	
250		0.790			0.760		0.767			0.698
248	0.819									
245			0.820	0.802		0.787		0.771	0.688	
240		0.796			0.767		0.774			0.708
238	0.825									
235			0.825	0.808		0.794		0.779	0.698	
230		0.803			0.775		0.781			0.707
228	0.830									

225			0.831	0.805		0.801		0.786	0.707	
220		0.809			0.782		0.789			0.726
218	0.836									
215			0.836	0.821		0.807		0.793	0.717	
210		0.816			0.790		0.796			0.736
208	0.842									
205			0.842	0.827		0.814		0.801	0.727	
200		0.823			0.798		0.803			0.746
198	0.847									
195			0.848	0.834		0.821		0.808	0.737	
190		0.829			0.805		0.811			0.755
188	0.853									
185			0.854	0.840		0.828		0.815	0.748	
180		0.836			0.813		0.818			0.765
178	0.858									
175			0.859	0.846		0.835		0.823	0.758	
170		0.842			0.821		0.825			0.775
168	0.864									
165			0.865	0.852		0.841		0.830	0.768	
160		0.849			0.828		0.833			0.785
158	0.869									
155			0.870	0.858		0.848		0.837	0.779	
150		0.855			0.836		0.840			0.794
148	0.875									
145			0.876	0.864		0.855		0.845	0.789	
140		0.862			0.843		0.847			0.804
138	0.880									
135			0.881	0.870		0.861		0.852	0.800	
130		0.868			0.850		0.854			0.814
128	0.885									
125			0.886	0.876		0.868		0.859	0.809	
120		0.874			0.858		0.861			0.823
118	0.890									
115			0.891	0.882		0.874		0.866	0.820	
110		0.880			0.865		0.868			0.833
108	0.895									
105			0.896	0.887		0.880		0.872	0.830	
100		0.886			0.872		0.875			0.842
98	0.900									
95			0.900	0.892		0.886		0.879	0.839	
90		0.891			0.878		0.881			
88	0.904									
85			0.905	0.897		0.891		0.885	0.849	
80		0.896			0.884		0.887			
78	0.908									
75			0.909	0.902		0.896		0.890	0.858	
70		0.901			0.890		0.892			
68	0.912									
65			0.912	0.906		0.901				
60		0.905			0.895		0.897			

58	0.915									
55			0.915	0.910		0.905				
50		0.909			0.900					
48	0.917									
45			0.918	0.913						
40		0.912								
38	0.920									
35			0.920	0.915						
30		0.914								
28	0.921									
25			0.922	0.917						
20		0.916								
18	0.923									
Recoil-free Fractions for Doublet 1_4, 14_23 Method										
T(K)	**$Fo_{89.5}$**	**Fo_{80}**	**Fo_{70}**	**Fo_{60}**	**Fo_{50}**	**Fo_{40}**	**Fo_{30}**	**Fo_{20}**	**Fo_{10}**	**Fo_{0}**
290		0.850			0.854		0.849			0.825
285			0.857	0.850		0.867		0.851	0.856	
283.1	0.852									
280		0.854			0.858		0.853			0.830
275			0.857	0.854		0.871		0.855	0.862	
273.1	0.856									
270		0.859			0.862		0.857			0.835
265			0.860	0.858		0.874		0.859	0.866	
263.1	0.860									
260		0.863			0.866		0.861			0.839
255			0.864	0.862		0.878		0.863	0.869	
253.1	0.864									
250		0.867			0.870		0.865			0.844
245			0.868	0.866		0.882		0.867	0.873	
243.1	0.868									
240		0.871			0.874		0.869			0.849
235			0.872	0.870		0.885		0.871	0.877	
233.1	0.872									
230		0.875			0.878		0.873			0.854
225			0.876	0.874		0.889		0.875	0.881	
223.1	0.876									
220		0.878			0.882		0.877			0.858
215			0.880	0.878		0.892		0.879	0.885	
213.1	0.880									
210		0.882			0.885		0.881			0.863
205			0.884	0.882		0.895		0.883	0.888	
203.1	0.884									
200		0.886			0.889		0.885			0.868
195			0.887	0.886		0.899		0.887	0.892	
193.1	0.888									
190		0.890			0.893		0.889			0.872
185			0.891	0.890		0.902		0.891	0.896	
183.1	0.892									
180		0.894			0.897		0.893			0.877
175			0.895	0.894		0.906		0.895	0.899	

173.1	0.896									
170		0.898			0.900		0.897			0.882
165			0.899	0.898		0.909		0.899	0.903	
163.1	0.900									
160		0.901			0.904		0.901			0.886
155			0.902	0.902		0.912		0.903	0.906	
153.1	0.903									
150		0.905			0.907		0.904			0.891
145			0.906	0.905		0.915		0.906	0.910	
143.1	0.907									
140		0.908			0.911		0.908			0.895
135			0.909	0.909		0.918		0.909	0.913	
133.1	0.910									
130		0.912			0.914		0.911			0.899
125			0.912	0.912		0.921		0.913	0.916	
123.1	0.914									
120		0.915			0.917		0.914			0.903
115			0.916	0.915		0.923		0.916	0.919	
113.1	0.917									
110		0.918			0.920		0.918			0.907
105			0.919	0.919		0.926		0.919	0.922	
103.1	0.920									
100		0.921			0.923		0.921			0.911
95			0.921	0.921		0.928		0.922	0.925	
93.1	0.923									
90		0.924			0.925		0.923			
85			0.924	0.924		0.931		0.925	0.927	
83.1	0.925									
80		0.926			0.928		0.926			
75			0.927	0.927		0.933		0.927	0.929	
73.1	0.928									
70		0.929			0.930		0.928			
65			0.929	0.929		0.934				
63.1	0.930									
60		0.931			0.932		0.930			
55			0.931	0.931		0.936				
53.1	0.931									
50		0.932			0.933					
45			0.933	0.932						
43.1	0.933									
40		0.934								
35			0.934	0.933						
33.1	0.934									
30		0.935								
25			0.935	0.934						
23.1	0.935									
20		0.935								
13.1	0.936									
Recoil-free Fractions for Doublet 2_3, 14_23 Method										
T(K)	**$Fo_{89.5}$**	**Fo_{80}**	**Fo_{70}**	**Fo_{60}**	**Fo_{50}**	**Fo_{40}**	**Fo_{30}**	**Fo_{20}**	**Fo_{10}**	**Fo_{0}**

290		0.722			0.680		0.706			0.502
288	0.754									
285			0.731	0.717		0.716		0.666	0.619	
280		0.729			0.688		0.714			0.514
278	0.760									
275			0.739	0.725		0.723		0.675	0.629	
270		0.737			0.697		0.722			0.526
268	0.767									
265			0.746	0.733		0.732		0.684	0.639	
260		0.744			0.706		0.730			0.538
258	0.774									
255			0.754	0.741		0.740		0.693	0.650	
250		0.752			0.714		0.738			0.550
248	0781									
245			0.761	0.748		0.747		0.702	0.660	
240		0.760			0.723		0.746			0.563
238	0.788									
235			0.769	0.756		0.755		0.712	0.670	
230		0.768			0.732		0.754			0.576
228	0.795									
225			0.777	0.764		0.763		0.721	0.681	
220		0.775			0.741		0.762			0.589
218	0.802									
215			0.784	0.773		0.772		0.731	0.691	
210		0.783			0.750		0.771			0.602
208	0.809									
205			0.792	0.781		0.780		0.740	0.703	
200		0.791			0.759		0.779			0.616
198	0.816									
195			0.800	0.789		0.788		0.750	0.714	
190		0.799			0.768		0.788			0.630
188	0.822									
185			0.807	0.797		0.796		0.760	0.725	
180		0.807			0.777		0.796			0.644
178	0.829									
175			0.815	0.805		0.804		0.769	0.736	
170		0.815			0.787		0.804			0.659
168	0.836									
165			0.823	0.813		0.812		0.779	0.747	
160		0.823			0.796		0.813			0.673
158	0.843									
155			0.830	0.821		0.821		0.789	0.758	
150		0.830			0.805		0.821			0.688
148	0.850									
145			0.838	0.829		0.829		0.799	0.770	
140		0.838			0.814		0.829			0.703
138	0.857									
135			0.845	0.837		0.837		0.808	0.781	
130		0.846			0.823		0.837			0.719
128	0.863									

125			0.853	0.845		0.845		0.818	0.792	
120		0.853			0.832		0.846			0.734
118	0.870									
115			0.860	0.853		0.853		0.828	0.804	
110		0.861			0.841		0.853			0.749
108	0.876									
105			0.867	0.861		0.860		0.837	0.815	
100		0.867			0.850		0.861			0.765
98	0.882									
95			0.874	0.868		0.867		0.846	0.826	
90		0.874			0.858		0.869			
88	0.888									
85			0.880	0.875		0.874		0.855	0.836	
80		0.881			0.866		0.876			
78	0.893									
75			0.886	0.881		0.881		0.864	0.847	
70		0.887			0.874		0.882			
68	0.898									
65			0.892	0.888		0.887				
60		0.893			0.880		0.888			
58	0.902									
55			0.897	0.893		0.893				
50		0.897			0.887					
48	0.906									
45			0.901	0.898						
40		0.902								
38	0.909									
35			0.905	0.901						
30		0.905								
28	0.912									
25			0.907	0.904						
20		0.907								
18	0.913									

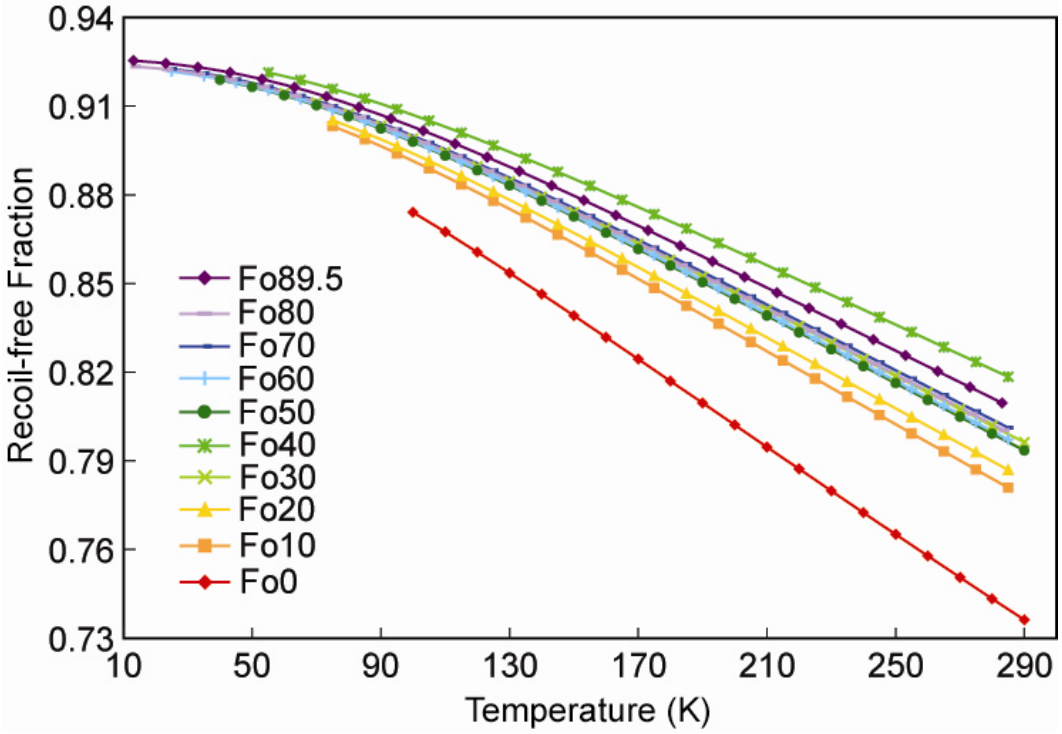

Figure 4.11; Recoil-free fraction vs. temperature for one doublet fits.

Table 4.4; Recoil-free fractions across the 13K-293K temperature range for one doublet fits. The recoil-free fraction, a ratio, is dimensionless. The gaps in the tables are an artifact of the fixed step size of the program calculating the recoil-free fractions.

Recoil-free Fractions for One Doublet Fits										
T(K)	**$Fo_{89.5}$**	**Fo_{80}**	**Fo_{70}**	**Fo_{60}**	**Fo_{50}**	**Fo_{40}**	**Fo_{30}**	**Fo_{20}**	**Fo_{10}**	**Fo_{0}**
290					0.794		0.796			0.736
285			0.801	0.797		0.818		0.787	0.781	
283.8		0.800								
283.1	0.809									
280					0.799		0.802			0.743
275			0.807	0.803		0.814		0.793	0.787	
273.8		0.806								
273.1	0.815									
270					0.805		0.807			0.751
265			0.812	0.809		0.819		0.799	0.793	
263.8		0.812								
263.1	0.820									
260					0.811		0.813			0.758
255			0.818	0.814		0.834		0.805	0.799	
253.8		0.817								
253.1	0.826									
250					0.816		0.819			0.765
245			0.823	0.820		0.839		0.812	0.806	

243.8		0.823								
243.1	0.831									
240					0.822		0.824			0.773
235			0.829	0.826		0.844		0.817	0.812	
233.8		0.828								
233.1	0.836									
230					0.828		0.830			0.780
225			0.835	0.831		0.849		0.823	0.818	
223.8		0.834								
223.1	0.842									
220					0.833		0.836			0.787
215			0.840	0.837		0.854		0.829	0.824	
213.8		0.840								
213.1	0.847									
210					0.839		0.841			0.795
205			0.846	0.843		0.859		0.835	0.830	
203.8		0.845								
203.1	0.852									
200					0.845		0.847			0.802
195			0.851	0.848		0.864		0.841	0.836	
193.8		0.851								
193.1	0.858									
190					0.850		0.852			0.810
185			0.857	0.854		0.869		0.847	0.842	
183.8		0.856								
183.1	0.863									
180					0.856		0.858			0.817
175			0.862	0.860		0.874		0.853	0.849	
173.8		0.862								
173.1	0.867									
170					0.862		0.863			0.824
165			0.867	0.865		0.878		0.858	0.855	
163.8		0.867								
163.1	0.873									
160					0.867		0.869			0.832
155			0.873	0.870		0.883		0.864	0.861	
153.8		0.873								
153.1	0.878									
150					0.873		0.874			0.839
145			0.878	0.876		0.888		0.870	0.867	
143.8		0.878								
143.1	0.883									
140					0.878		0.879			0.846
135			0.883	0.881		0.893		0.876	0.872	
133.8		0.883								
133.1	0.888									
130					0.883		0.885			0.854
125			0.888	0.886		0.898		0.881	0.878	
123.8		0.888								
123.1	0.893									

120					0.888		0.890			0.861
115			0.893	0.891		0.901		0.886	0.884	
113.8		0.893								
113.1	0.897									
110					0.893		0.894			0.868
105			0.898	0.896		0.905		0.892	0.889	
103.8		0.898								
103.1	0.902									
100					0.898		0.899			0.874
95			0.902	0.901		0.909		0.896	0.894	
93.8		0.902								
93.1	0.906									
90					0.902		0.903			
85			0.906	0.905		0.913		0.901	0.899	
83.8		0.906								
83.1	0.910									
80					0.907		0.907			
75			0.910	0.909		0.916		0.905	0.903	
73.8		0.910								
73.1	0.913									
70					0.910		0.911			
65			0.914	0.912		0.919				
63.8		0.913								
63.1	0.916									
60					0.914		0.914			
55			0.917	0.915		0.921				
53.8		0.916								
53.1	0.919									
50					0.917					
45			0.919	0.918						
43.8		0.919								
43.1	0.921									
40					0.919					
35			0.921	0.920						
33.8		0.921								
33.1	0.923									
30										
25			0.923	0.922						
23.8		0.922								
23.1	0.925									
13.8										
13.1	0.925									
		0.923								

The recoil-free fraction calculation also yields values for the characteristic Mössbauer temperature Θ_M and the intrinsic isomer shift (δ_1 equation 2.14), the temperature independent isomer shift. Those data, as presented in Figures 4.12 and 4.13 and Table 4.5, do not show smooth trends.

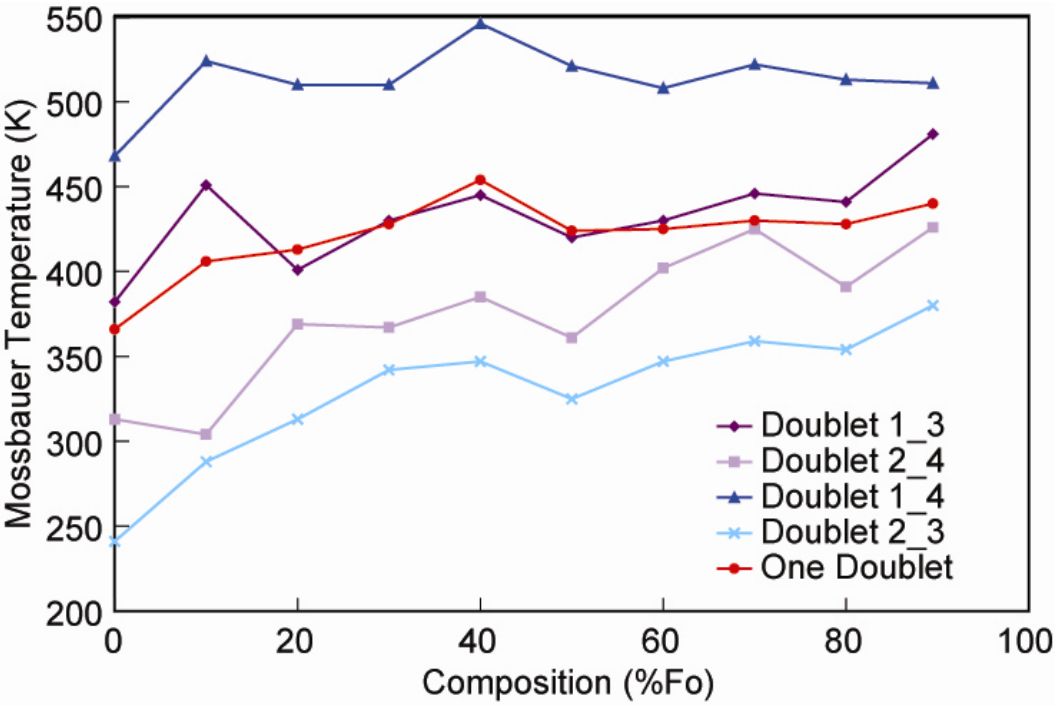

Figure 4.12; Characteristic Mössbauer temperature (in K) vs. olivine composition for one doublet fitting method and both two doublet, correlated width fitting methods. The one doublet method is shown in red, the 13_24 method doublets are shown in purple and the 14_23 method doublets are shown in blue.

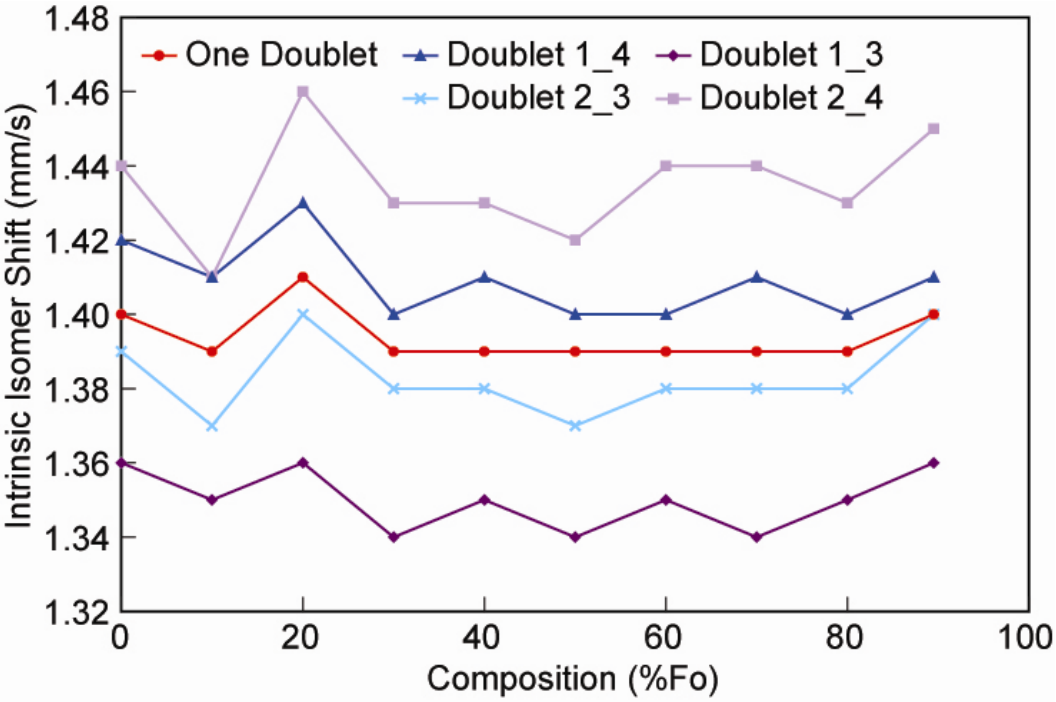

Figure 4.13; Intrinsic isomer shift (in mm/s) vs. olivine composition for one doublet fitting method and both two doublet, correlated width fitting methods. The one doublet method is shown in red, the 13_24 method doublets are shown in purple and the 14_23 method doublets are shown in blue. Note that Fo_{20} has anomalously high isomer shift values.

Table 4.5; Characteristic Mössbauer temperatures and intrinsic isomer shifts for one doublet and both two doublet fitting methods.

Characteristic Mössbauer Temperature and Intrinsic Isomer Shift Values										
	Θ_M (K)				δ_1 (mm/s)				Θ_M	δ_1
	13_24 Method		14_23 Method		13_24 Method		14_23 Method		One Doublet	
	1_3	2_4	1_4	2_3	1_3	2_4	1_4	2_3		
Fo0	382	313	468	241	1.36	1.44	1.42	1.39	366	1.40
Fo10	451	304	524	288	1.35	1.41	1.41	1.37	406	1.39
Fo20	401	369	510	313	1.36	1.46	1.43	1.40	413	1.41
Fo30	430	367	510	342	1.34	1.43	1.40	1.38	428	1.39
Fo40	445	385	546	347	1.35	1.43	1.41	1.38	454	1.39
Fo50	420	361	521	325	1.34	1.42	1.40	1.37	424	1.39
Fo60	430	402	508	347	1.35	1.44	1.40	1.38	425	1.39
Fo70	446	425	522	359	1.34	1.44	1.41	1.38	430	1.39
Fo80	441	391	513	354	1.35	1.43	1.40	1.38	428	1.39
Fo89.5	481	426	511	380	1.36	1.45	1.41	1.40	440	1.40

The last aspect of these synthetic olivine spectra that was examined was the magnetic ordering temperature. This is a particularly difficult value to determine, and slightly ambiguous to define, because magnetic ordering occurs over a range of temperatures. The kinetics of ordering are also unknown, i.e., time may also be a factor in how ordered a spectrum becomes. As magnetic ordering begins, the doublets first begin to broaden and reduce in intensity, and then irregular peak shapes arise as the nuclear energy levels lose degeneracy. Figure 4.14 shows these intermediate stages for Fo_{40}.

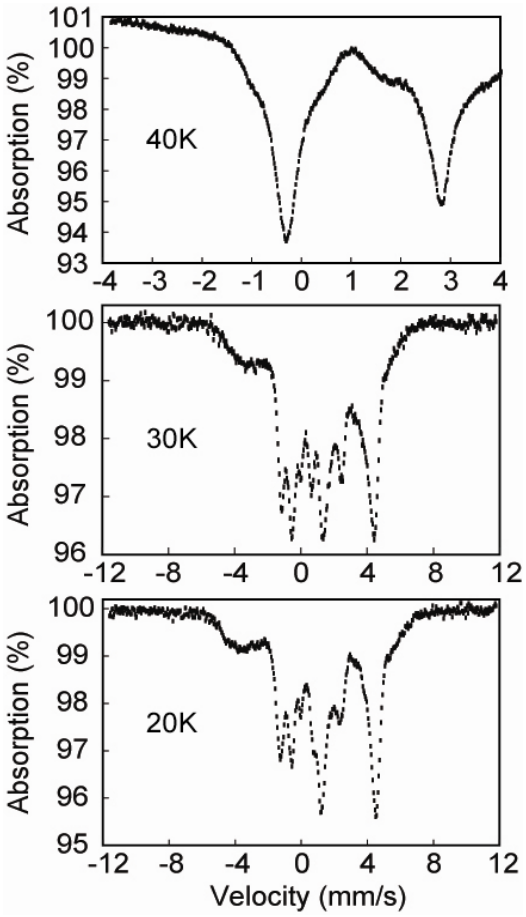

Figure 4.14; Magnetic ordering in Fo_{40} at 20, 30, and 40K.

These intermediate spectra are unfittable. After magnetic ordering is complete, a fittable but complicated spectrum appears. Below is a completely split Fo_0 spectrum at 20K for comparison.

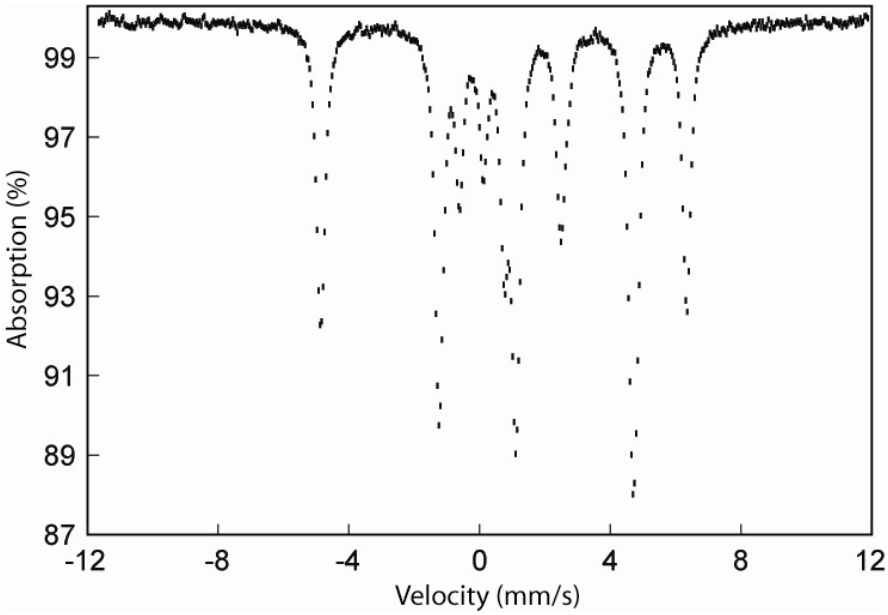

Figure 4.15; Magnetically split spectrum of fayalite (Fo_0) at 20K.

The problem of determining magnetic ordering temperature is further confused because impurities and/or ferric iron in the sample will change the ordering temperature and the spectral appearance as the sample orders. The data presented here are, therefore, a first estimate of the temperature at which ordering begins. For comparison, the Menzies set of synthetic olivine samples is shown on the same plot. The other set of samples was incompletely reacted and many of the compositions contained ferric iron and other impurities. The magnetic ordering temperature is, however, much more closely constrained for those samples. Note that not all compositions are shown. The compositions that do not appear on the

graph are those in which magnetic ordering occurs below 12K. We do not yet have data in that temperature range for these samples.

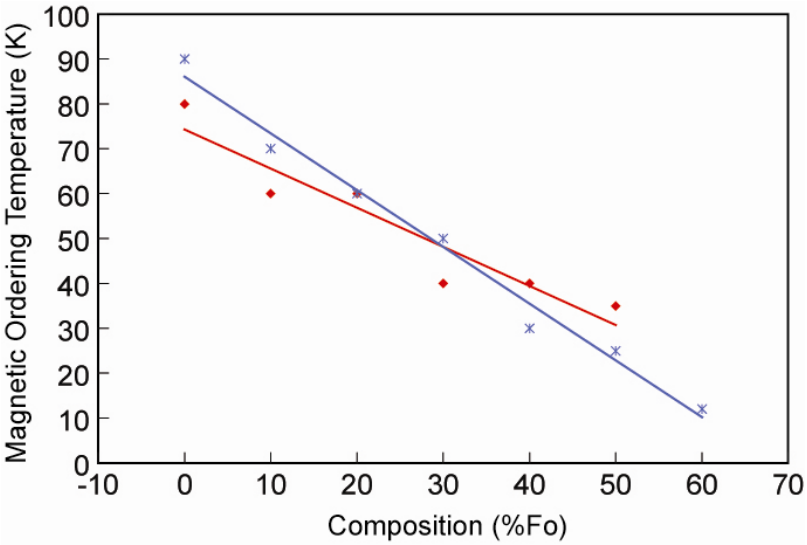

Figure 4.16; Magnetic ordering temperature in K vs. olivine composition in %Fo for Menzies synthetic samples (blue) and Lindsley synthetic samples (red).

More work is intended in all areas of this study. Specifically, high and low temperature data are being acquired for all compositions listed in this study as well as full runs on intermediate compositions.

Chapter 5

Discussion, Implications, and Conclusion

The first question that this study set out to answer was how the Fe in olivine was ordered between the two non-equivalent octahedral sites in olivine. The spectroscopic study of olivine did indeed show that two doublets were needed to attain an acceptable fit for an olivine Mössbauer spectrum. These two doublets were arranged in the 13_24 configuration and the 14_23 configuration. To ascertain which fitting method best represented the olivine structure several techniques were used: the χ^2 values of these two methods were compared, isomer shift vs. temperature and quadrupole splitting vs. temperature trends were examined for smoothness, and doublet area ratios were also examined. The admittedly disappointing conclusions to these investigations are that

1. There is no way, at this time, to tell the two fitting methods apart;
2. Even though two doublets are easily resolved, they cannot be assigned to the M1 and M2 sites at this time, and may very well not be related to the sites at all.

The second conclusion, in some ways, makes the first conclusion irrelevant. The results showed that the area ratios for the two doublets, when the doublet widths were allowed to vary independently of one another, were incompatible

with known facts about the olivine structure. Fo_0, having no magnesium content, should show iron evenly distributed between the two sites. The area ratios in the two doublet fits of Fo_0 in this study were ~70:30 for both fitting methods. Also, there was no trend associated with the doublet areas. If there were any observable ordering, then as the Mg:Fe ratio changed, there should be a systematic change in the doublet ratios. This could mean, simply, that the peaks have extensive enough overlap at these temperatures that the fitting program cannot produce a unique fit. The implications, however, are more extensive. The results showed that when the areas of the two doublets were correlated (constrained to vary together), the isomer shift vs. temperature and quadrupole splitting vs. temperature curves became smoother and more systematic. In effect, the areas of the doublet are related to the isomer shift and quadrupole splitting values. Because the areas are not representative of the real site occupancies in the structure, doubt is raised about the integrity of the other parameters.

Here there arises a bit of a conundrum; the one doublet fits do not accurately represent the data, but the two doublet fits provide great uncertainty in the parameters. The logical resolution to this dilemma is to acquire higher and lower temperature data on these samples. At higher temperatures, the two doublets are separated by a greater degree, and may be more easily resolved. At lower temperatures, the spectrum is re-ordered into two sextets. Both of these scenarios will allow for refinement of the site parameters and will help resolve both the problem of the fitting method and the problem of the site assignment.

Fortunately, these samples are currently being run at high temperatures, and low temperature data, down to 4.2K will be acquired in the near future.

In light of the uncertainty in the two doublet fits, one doublet fits were performed on all spectra. While these fits are not adequate for the data quality of these spectra, they are an essential part of the study. In a great number of analytical situations, peak overlap with other minerals and low resolution makes two doublet olivine fits impossible. The one doublet parameters are, therefore, an essential addition to the Mössbauer spectroscopic library. They also have provided useful insight into the trends analyzed in the second section of this study.

The second question that this study addressed was how isomer shift and quadrupole splitting varied with olivine composition. Isomer shift proved incredibly consistent over the composition range, never varying outside the error bars for the technique for one doublet or two doublet fits. In all fitting methods (one doublet and both two doublet), three compositions showed consistently higher isomer shift values. These compositions are Fo_0, Fo_{20} and $Fo_{89.5}$. The Fo_{20} composition, in most cases, showed the highest isomer shift values. This is possibly a bad data run, and a re-run is planned for the future. However, the Menzies Fo_{20} sample showed similarly high isomer shift values. For the 295, 270, and 245K spectra, the isomer shifts were 1.23, 1.21, and 1.23 mm/s respectively for a one doublet fit. Other compositions from the Menzies suite of samples were also in fair agreement with the Lindsley sample parameters. For instance, the

Menzies Fo_{70} sample had isomer shifts of 1.16, 1.18, and 1.21 mm/s for 295, 270, and 245K respectively. It is hard to say anything conclusive about these trends because they are almost within the error bars for the technique for the Lindsley samples and within the error bars for the Menzies samples. Perhaps the introduction of the high and low temperature data to the picture will provide clarification.

Quadrupole splitting variation with composition, an idea first proposed by Philip Bland and Olwyn Menzies in 2001, seems to be the diagnostic jackpot. Both the one and two doublet fits show a clear trend in quadrupole splitting with composition, which is diagnostic to within ± 20% absolute forsterite. The relationship between quadrupole splitting and composition becomes quite important when analyzing spectra from remote sources, such as the Martian surface. Below is a Martian spectrum from Morris et al. (2006) as well as a fit of the same data from our lab.

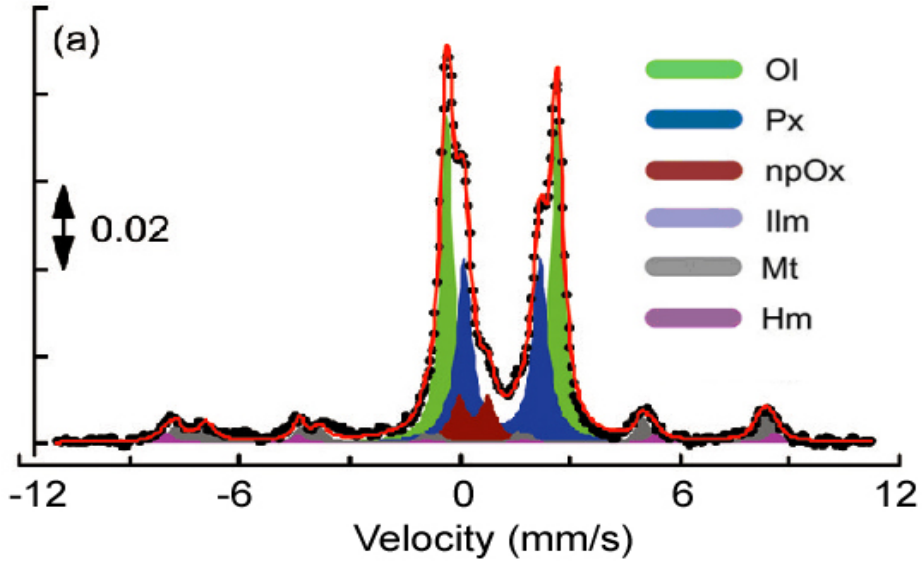

Figure 5.1; Adirondac class MER spectrum processed and fit by Morris et al. (2006). The spectrum is in the temperature range of 210-270K.

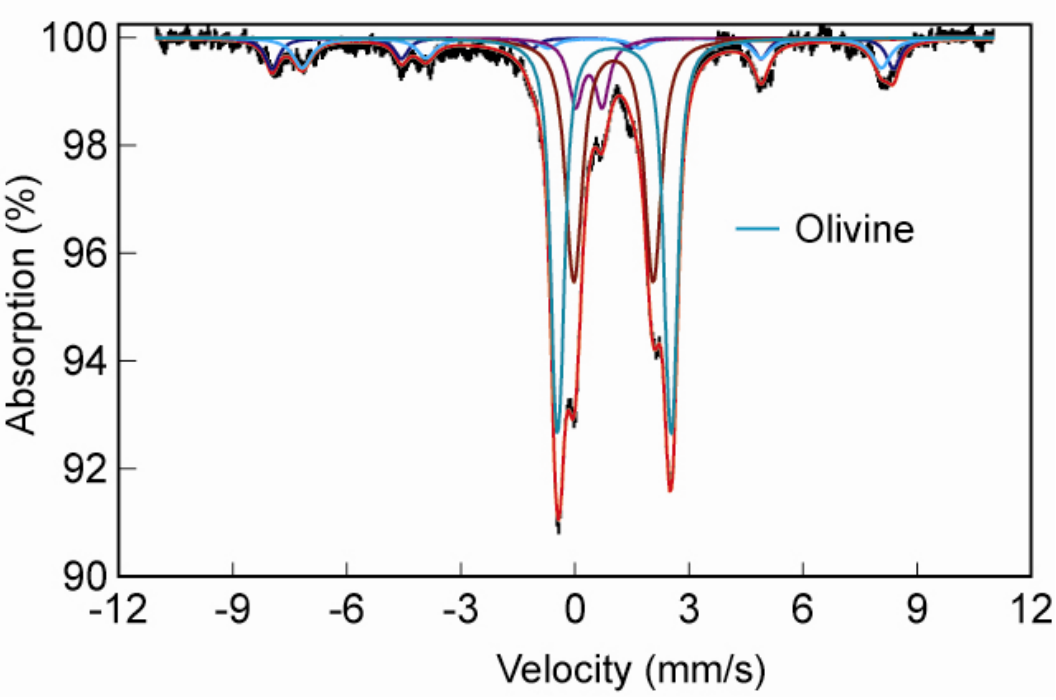

Figure 5.2; The same MER A Adirondac summed spectra from sol 18, 33, and 34. Data were inverted to transmission form to accommodate our fitting software. Temperature range of 210-270K. Fit performed by Yarrow Rothstein.

Because of diurnal temperature variations on the Martian surface, spectra are acquired while the temperature is changing. This is equivalent to averaging the Mössbauer parameter values of discrete temperature spectra across that range. The parameters of olivine in the Morris et al. (2006) study are 1.16 mm/s isomer shift and 2.99 mm/s quadrupole splitting. Our own study of the exact same Adirondac class spectra gave values of 1.15 mm/s isomer shift and 3.14 mm/s quadrupole splitting. Although the isomer shifts are comparable, the quadrupole splitting values are very different, and lead to contrasting compositional conclusions. The Morris et al. (2006) QS value would indicate that this olivine is almost pure forsterite where the values from our lab would indicate almost pure fayalite. It is clear that further work needs to be done in this area as well.

The third question that this study investigated is how the magnetic ordering temperature in olivine is related to composition. The magnetic ordering temperature proved difficult to document because it is not sufficiently well defined in our experiments. Magnetic ordering temperature could be classified as the temperature at which the doublets begin to broaden and decrease in intensity, the temperature when ordering is complete, or it could be defined as the range of temperatures across which re-ordering takes place. This lack of specificity and the time constraints on the project itself led to insufficient precision in these measurements.

Both the Menzies and the Lindsley samples do show a linear correlation between magnetic ordering temperature and composition, but the slopes of the

best-fit lines were not the same. This could be due to many factors: the imprecision listed above, impurities in the samples, and the presence of ferric iron. It is clear that more work must be done to determine if the trend is predictable in a diagnostically useful manner.

Previously, the magnetic splitting process of samples was not a pursuit that was given much time, as these spectra are unfittable. However, it seems that interesting aspects of the kinetics of the ordering process may be accessible through a closer look at this process. To further this piece of the investigation, several aspects of ordering could be studied as follows. The exact onset temperature of magnetic ordering of each composition could be documented by systematic reductions in temperature with a small temperature increment, say 3-5K. The spectra of the intermediate stages in the ordering process could be studied to see if there are any specific spectral shifts that can be attributed to one site ordering before the other. This could be done again by a systematic temperature reduction with small temperature increments. The end point of the ordering process could be accurately established for each composition establishing a temperature range over which the process occurs. This range may also be compositionally dependent. Also, ranging runtimes could be applied to intermediate stages of magnetic ordering to determine if reaction kinetics are affecting the spectral product. In other words, it could be determined if increasing the runtime increases the degree of ordering.

Unfortunately, more work in this area is not of high priority in the continuation of this study. The applications for such a correlation are fairly limited, even though the subject is intriguing. Olivine's highest magnetic ordering temperature is less than 100K. The surface temperature of Mars is, on average, 120K higher than that. Since Mössbauer spectroscopy is not a mineralogical identification tool in and of itself, and because the technique is limited by the radioactive decay of the source, there is very little likelihood that Mössbauer spectroscopy will be used on planets where magnetic ordering temperatures are reached. However, in low temperature, mixed mineral spectra, the magnetic parameters of olivine are important if discrimination of multiple magnetically split species is required, so low temperature investigations on olivine will continue.

The fourth goal of this study was to compare olivine Mössbauer parameters to those for other ferromagnetic species. Completely cataloguing olivine Mössbauer parameters across temperature and composition ranges was a necessary part of this pursuit. Olivine has a characteristically high quadrupole splitting with an isomer shift that is typical of many silicate and other minerals containing Fe^{2+} in octahedral coordination. Currently, the minerals that most closely match olivine parameters are the sulfates. Table 5.1 shows a variety of sulfate parameters at 295K.

Table 5.1; Mössbauer parameters for some ferrous sulfates at 295K and various compositions of olivine at 293K. Only sulfate ferrous doublets parameters are shown.

295K Ferrous Sulfate Parameters					
Mineral	Sample #	δ (mm/s)	Δ (mm/s)	δ (mm/s)	Δ (mm/s)
Szomolnokite	S60	1.31	2.90	1.31	3.31
Rozenite	JB626B	1.32	2.94	1.36	3.12
Romerite	SPT110	1.27	2.83		
Melanterite	SPT130	1.27	3.33		
Tochilinite	TOC101	1.17	2.82		
Halotrichite	VZO128	1.29	2.72	1.30	3.35
Olivine Parameters					
Composition	Fitting Method	δ (mm/s)	Δ (mm/s)	δ (mm/s)	Δ (mm/s)
Fo_0	13_24	1.12	2.85	1.22	2.89
	14_23	1.18	2.96	1.16	2.76
	one doublet	1.17	2.87		
Fo_{50}	13_24	1.10	2.91	1.20	2.95
	14_23	1.16	3.02	1.14	2.82
	one doublet	1.15	2.93		
$Fo_{89.5}$	13_24	1.12	3.01	1.22	3.03
	14_23	1.17	3.12	1.16	2.93
	one doublet	1.17	3.02		

The values of tochilinite are the closest to those of olivine. However, low resolution and peak overlap can make these species much more difficult to differentiate.

To date, there are hundreds of sulfate mineral species that have never been analyzed, or have been analyzed only at room temperature, using Mössbauer spectroscopy. An additional study that is planned for next year comes out of this need. Currently, over one hundred sulfates, both ferric and ferrous, are awaiting runtime. The hope is that information on a wide variety of sulfate and olivine compositions will either make distinctions easier between these species in rock spectra, or help the Mössbauer community make informed decisions about

interpretations of Mössbauer parameters with fair knowledge of the limitations of the technique.

Finally, this study set out to catalogue the recoil-free fraction values for olivine across both composition and temperature so that these data could be used in the future to correct for area ratios in rock spectra. Those data have been determined and show nonsystematic variation, confirming the necessity to measure them for multiple compositions within given mineral species. Struggling with the assumptions and justifications used to acquire the recoil-free fraction data has led to a new project that will investigate area ratios in a novel and empirical manner. It will be fascinating to see how these two methods compare.

As with any in-depth investigation, this study has led to more questions than answers. Many questions were, indeed raised by this study. There is now a solid place from which to proceed. Acquiring complete and careful data for synthetic samples can often seem like a daunting task. This is how we explore our world. We see in nature, we test in the lab, and then we find patterns, draw conclusions and understand more fully the amazing processes of Earth and other planets.

Works Cited

Amthauer G, Annersten H, and Hafner SS. 1976. The Mössbauer spectrum of ^{57}Fe in silicate garnets. *Z. Kristallogr.* 143: 14-55.

Annersten H, Ericsson T, and Filippidis A. 1982. Cation ordering in Ni-Fe olivine. *Am. Mineral.* 67: 1212-17.

Annersten H, Jacob A, and Filippidis, A. 1984. Cation ordering in Fe-Mn silicate olivines. *Am. Mineral.* 69: 1110-15.

Artioli G, Rinaldi R, Wilson CC, Zanazzi PF. 1995. High-temperature Fe-Mg cation partitioning in olivine: In-situ single-crystal neutron diffraction study. *Am. Mineral.* 80: 197-200.

Bancroft GM. 1973. *Mössbauer Spectroscopy. An Introduction for Inorganic and Chemists and Geochemists.* New York: McGraw Hill.

Bancroft GM and Brown JR. 1975. A Mössbauer study of coexisting hornblendes and biotites: Quantitative Fe^{3+}/Fe^{2+} ratios. *Am. Mineral.* 60:265-72

Bish DL. 1981. Cation ordering in synthetic and natural Ni-Mg olivine. *Am. Mineral.* 66: 770-76.

Bragg WL and Brown GB. 1926. Die struktur des olivins. *Z. Kristallogr.* 63: 538-56.

Brown GE and Prewitt CT. 1973. High temperature crystal chemistry of hortonolite. *Am. Mineral.* 58: 577-87.

Brown, G.E. 1980. Olivines and Silicate Spinels. In P.H. Ribbe, Ed.,

Orthosilicates. Reviews in Mineralogy. p. 275-381. Mineralogical Society of America. Washington, D.C.

Burns RG. 1993. *Mineralogical Applications of Crystal Field Theory 2nd Ed.* Cambridge University Press: New York. 551p.

Bush WR, Hafner SS, and Virgo D. 1970. Some ordering of iron and magnesium at the octahedrally coordinated sites in a magnesium-rich olivine. *Nature* 227: 1339-41.

De Grave E, Verbeek AE, and Chambaere DG. 1985. Influence of small aluminum substitutions on the hematite lattice. *Phys. Let.* 107A: 181-84.

De Grave E and van Alboom AV. 1991. Evaluation of ferrous and ferric Mössbauer fractions. *Phys. Chem. Miner.* 18: 337-42.

Dyar MD. 1984. Precision and interlaboratory reproducibility of measurements of the Mössbauer effect in minerals. *Am. Mineral.* 69:1127-44.

Dyar MD, Agresti DG, Scaefer MW, Grant CA, and Sklute EC. 2006. Mössbauer Spectroscopy of Earth and Planetary Materials. *Ann. Rev. Earth Planet. Sci.* 34: 83-125.

Frauenfelder H. 1962. *The Mössbauer Effect.* New York: WA Benjamin. 333pp.

Ghose S. 1962. The nature of Mg^{2+}-Fe^{2+} distribution in some ferromagnesian silicate minerals. *Am. Mineral.* 47: 388-94.

Goncharenko AI et al.. 1995. Investigation of plastically deformed olivines from ultramafites using Mössbauer spectroscopy. *T. Rus. Acad. Sci./Earth Sci. Sect.* 357: 1213-14.

Grant CA. 1995. *Sources of Experimental and Analytical Error in Measurements of the Mössbauer Effect in Amphibole.* PhD thesis. University of Oregon. 213p.

Greenwood NB and Gibb TC. 1971. *Mössbauer Spectroscopy*. London: Chapman and Hall. 45pp.

Lipkin HJ. 1960. Some simple features of the Mössbauer effect. *Ann. Phys.* 9: 332-39.

Lumpkin GR and Ribbe PH. 1983. Composition, order-disorder and lattice parameters of olivines: relationships in silicate, germate, beryllate, phosphate and borate olivines. *Amer. Mineral.* 68: 164-76.

Malysheva TV, Kurash VV, and Yermakov AN. 1969. Mössbauer analysis of substitution of Fe^{2+} for Mg in olivines. *Geochem. Int.*+ 6: 1101-04.

Margulies S abd Ehrman JR. 1961. Transmission and line broadening of resonance radiation incident on a resonant absorber. *Nuc. Instrum. Methods* 12: 131-37.

Menzies ON, Bland PA, Berry FJ. 2001. An ^{57}Fe Moessbauer study of the olivine solid solution series; implications for meteorite classification and deconvolution of unequilibrated chondrite spectra. *Lunar and planetary science, XXXII; Papers presented to the Thirty-second lunar and planetary science conference. Abstracts of Papers Submitted to the Lunar and Planetary Science Conference* 32 abstr. no. 1622.

Morozov M et al.. 2005. Octahedral cation partitioning in Mg, Fe^{2+}-olivine.

Mössbauer spectroscopic study of synthetic $(Mg_{0.5}Fe^{2+}_{0.5})_2SiO_4$ (Fa_{50}). *Eur. J. Mineral.* 17: 495-500.

Morris RV et al.. 2004. Mineralogy at Gusev crater from Mössbauer spectrometer on the Spirit rover. *Science* 305: 833-36.

Morris RV et al.. 2006. Mössbauer mineralogy of rock, soil, and dust at Gusev crater, Mars: Spirit's journey through weakly altered olivine basalt on the plains and pervasively altered basalt in the Columbia Hills. *J. Geophys. Res. – Planet.* 11: E02S13

Mørup S and Both E. 1975. Interpretation of Mössbauer spectra with broadened lines. *Nuc. Instrum. Methods* 124: 445-48.

Mössbauer RL. 1958. Kernresonanzfluoreszenz von Gammastrahlung in Ir^{191}. *Zeits. Phys.* 151: 124-43.

Murad E and Cashion J. 2004. *Mössbauer Spectroscopy of Environmental Materials and their Industrial Utilization*. Dordrecht: Kluwer. 417pp.

Nikitina LP, Grebenshikov RG, and Ovchinnikov NO. 1982. Atomic ordering in silicates and germates of olivine and pyroxene structure. *Phys. of Min. and Ore Microscopy. – IMA* 13: 131-41.

Nord AG, Annersten H, and Filippidis A. 1982. The cation distribution in synthetic Mg-Fe-Ni olivines. *Am. Mineral.* 67: 1206-11.

Ottonello G, Della Giusta A, and Molin GM. 1989. Cation ordering in Ni-Mg olivines. *Am. Mineral.* 74: 411-21.

Ottonello G, Princivalle F, and Della Giusta A. 1990. Temperature, composition,

and f_{O_2} effects on intersite distribution of Mg and Fe^{2+} in olivine. *Phys. Chem. Minerals* 17: 301-12.

Princivalle F. 1990. Influence of temperature and composition on Mg-Fe^{2+} intracrystalline distribution in olivines. *Miner. Petrol.* 43: 121-29.

Rajamani V, Brown GE, and Prewitt CT. 1975. Cation ordering in Ni-Mg olivine. *Am. Mineral.* 60: 292-99.

Rancourt DG. 1994. Mössbauer spectroscopy of minerals I. Inadequacy of Lorentzian-line doublets in fitting spectra arising from quadrupole splitting distributions. *Phys. Chem. Minerals* 21:244-49

Rancourt DG. 1989. Accurate sit populations from Mössbauer spectroscopy. *Nuc. Instrum. Methods* B44: 199-210.

Rancourt DG, McDonald AM, Lalonde AE, and Ping JY. 1993. Mössbauer absorber thickness for accurate site populations in Fe-bearing minerals. *Am. Mineral.* 78: 1-7.

Redfern SAT et al.. 1998. Fe-Mn cation ordering in fayalite-tephroite $(Fe_xMn_{1-x})_2SiO_4$ olivines; a neutron diffraction study. *Mineral. Mag.* 62: 607-15.

Ruby SL and Hicks JM. 1962. Line shape in Mössbauer spectroscopy. *Rev. Sci. Instrum.* 33: 27-30.

Ruby SL. 1973. Why Misfit when you already have χ^2? In IJ Gruverman and CW Seidel, Eds., *Mössbauer Effect Methodology 8*, p. 263-276. Plenium Press: New York.

Shinno I. 1974. Mössbauer studies of olivine temperature dependence of the parameter and site identification of the spectra. *J. Jap. Assoc. Mineral., Pertrol., and Econ. Geol.* 69: 354-63.

Shinno I, Hayashi M, and Kuroda Y. 1974. Mössbauer studies of natural olivines. *Mineralogical Journal* 7: 344-58.

Vandenberghe RE, De Grave E, and Bakker PMA. 1994. On the methodology of the analysis of Mössbauer spectra. *Hyperfine Interact.* 83: 29-49.

Virgo D and Hafner SS. 1972. Temperature-dependent Mg, Fe distribution in lunar olivine. *Earth Planet Sci. Lett.* 14: 305-12.

Visscher WM. 1960. Study of lattice vibrations by resonant absorption of nuclear gamma rays. *Ann. Phys.* 9: 194-210.

Wegner H. 1965. *Der Mössbauer-Effekt und Seine Anwendung in Physik and Chemie.* Mannheim: Bibliogr. Institut. 214pp.

Wertheim G. 1968. *Mössbauer Effect: Principles and Applications*. New York: Academic Press. 116p.

Wivel C and Mørup S. 1981. Improved computational procedure for evaluation of overlapping hyperfine parameter distribution in Mössbauer spectra. *J. Phys. E. Sci. Instrum. 14*, 605-610.

Yupu Y. 1982. Mössbauer spectra of olivines and determination of the degree of order of Fe^{2+}, Mg. *Research in Geology* 1982: 230-37.